Nanoscale

Enhanced Photochemical Activity and Ultrafast Photocarrier Dynamics in Sustainable Synthetic Melanin Nanoparticle-Based Donor-Acceptor Inkjet-Printed Molecular Junctions

Journal:	*Nanoscale*
Manuscript ID	NR-ART-05-2023-002387.R1
Article Type:	Paper
Date Submitted by the Author:	30-Jul-2023
Complete List of Authors:	DeMarco, Max; Wake Forest University, Chemistry Ballard, Mathew; Wake Forest University, Chemistry Grage, Elinor; Wake Forest University, Chemistry Nourigheimasi, Farnoush; Wake Forest University, Chemistry Getter, Lillian; Wake Forest University, Chemistry Shafiee, Ashkan; Wake Forest Baptist Medical Center Ghadiri, Elham; Wake Forest University, Chemistry

Enhanced Photochemical Activity and Ultrafast Photocarrier Dynamics in Sustainable Synthetic Melanin Nanoparticle-Based Donor-Acceptor Inkjet-Printed Molecular Junctions

Max DeMarco[1], Matthew Ballard[1], Elinor Grage[1], Farnoush Nourigheimasi[1], Lillian Getter[1], Ashkan Shafiee[2,3], and Elham Ghadiri[1,2,3,*]

1. Chemistry Department, Wake Forest University
2. Wake Forest School of Medicine, Wake Forest University
3. Center for Functional Materials, Wake Forest University

* Author to whom any correspondence should be addressed. ghadire@wfu.edu

Abstract

Melanin is a stable, widely light-absorbing, photoactive, and biocompatible material viable for energy conversion, photocatalysis, and bioelectronic applications. To achieve multifunctional nanostructures, we synthesized melanin nanoparticles of uniform size and controlled chemical composition (dopamelanin and eumelanin) and used them with titanium dioxide to fabricate donor-acceptor bilayers. Their size enhances the surface-to-volume ratio important for any surface-mediated functionality, such as photocatalysis, sensing, and drug loading and release, while controlling their chemical composition enables us to control the film's functionality and reproducibility. Inkjet printing uniquely allowed to control the deposited amount of materials with minimum ink waste suitable for reproducible materials deposition. We studied the photochemical characteristics of the donor-acceptor melanin-TiO_2 nanostructured films via photocatalytic degradation of methylene blue dye under selective UV-NIR and Vis-NIR irradiation conditions. Under both irradiation conditions, they exhibited photocatalytic characteristics superior to pure melanin and, under UV-NIR irradiation, to TiO_2 alone; TiO_2 is photoactive only under UV irradiation. The enhanced photocatalytic characteristics of the melanin-TiO_2 nanostructured bilayer films, particularly when excited by visible light, point to charge separation at the melanin-TiO_2 interface as a possible mechanism. We performed ultrafast laser spectroscopy to investigate the photochemical characteristics of pure melanin and the melanin-TiO_2 constructs and found that their time-resolved photoexcited spectral patterns differ. We incorporated singular value decomposition analysis to quantitatively deconvolute and compare the dynamics of photochemical processes for melanin and melanin-TiO_2 heterostructures. This observation supports electronic interactions; namely, interfacial charge separation at the melanin and TiO_2 interface. The excited-state relaxation in melanin-TiO_2 increases markedly from 5 ps to 400 ps. The results are remarkable for the future intriguing application of melanin-based constructs for bioelectronics and energy conversion.

Keywords: melanin, bioelectronics, photocatalysis, photochemistry, ultrafast spectroscopy, eumelanin, dopamelanin, inkjet-printing

1. Introduction

Because of numerous potential applications, research interest in melanin pigment is raising. Melanin is a broad class of materials[1,2] that occur in different forms and are among the most abundant and stable natural biopigments. They are found in most living organisms, including in human skin[3], hair[4], eyes[5], and brain.[2] Eumelanin is a black-brownish pigment; pheomelanin is red; neuromelanin is generated by dopaminergic neurons in the brain; and dopamelanin is a synthetic form.[2] Melanin strongly absorbs ultraviolet (UV) photons, and its primary role in biological systems was narrowly understood as a photoprotectant.

The melanin family has unique but not well-understood physical and chemical characteristics. Melanin absorbs broadly, from the UV to near infrared (NIR) regions. Typically, the optical absorption of a well-dispersed melanin suspension is monotonic and featureless, with exponential dependence upon wavelength.

The electrical conductivity of DOPA-derived melanin films and pelletized powders was shown to depend strongly on the hydration state of the material.[6] Melanins are photoconductive in the solid state; that is, their resistance decreases under UV or visible light.[6,7] They also show water-dependent conductivity, once described by an amorphous semiconductor model and recently attributed to a combination of ion and electrical conduction. Electron paramagnetic resonance (EPR) spectroscopy and DC electrical measurements have been performed to clarify these observations. Hydrated-phase melanin's EPR signal increases under steady-state irradiation with visible and near-UV light. A photocurrent is generated when eumelanin is irradiated with UV, and the electrical conductivity strongly depends on the hydration state of the pigment. Moreover, free-radical scavenging behavior[8,9] and antioxidant properties have been reported for melanin.[10]

These unique physical and chemical properties indicate that the broad material class of melanins may be valuable for applications ranging from biocompatible bioelectronics to energy conversion. However, integrating them will require, first, controlling their structure and chemical composition through synthesis. The main limitations of melanin pigments extracted from biological sources are their structural and chemical diversity and the variety and abundance of metal cations, which are associated with proteins and other biological components, and persist throughout the isolation and drying procedures. These features prevent a detailed characterization of the pigment and its value for different applications. Second, we have limited knowledge about melanin's electronic, optoelectronic, and photochemical characteristics; more specifically, fundamental aspects of electron-transfer processes. The problem with many biopigments is poor electronic and charge-transport properties. Therefore, future applications depend on a thorough understanding of melanin's photochemistry and electronic characteristics. Third, the practical design of melanin or melanin-based heterostructures for incorporation into electronic, optoelectronic, or energy-conversion devices remains undocumented.

Printing technologies have been employed in applications ranging from electronic devices, including transistors[11,12], light-emitting diodes[13], and solar cells[14], to biofabrication[15,16], tissue engineering[17,18], bioelectronics[19–21], and drug delivery[22–24]. Inkjet printing allows the precise, computer-controlled deposition of materials for thin films or devices with minimal ink waste. We used it to deposit melanin nanoparticles in a uniform surface for drug-loading applications.[22]

Here, we report on our synthesis of melanin and melanin-based heterostructures in which the size and chemical composition of the nanoparticles is controlled and reproducible. We synthesize two types of melanin nanoparticles considered as sub-classes of eumelanin with different starting

chemicals. We then integrate them with large-bandgap TiO_2 to form donor-acceptor-based heterojunctions resembling a sensitized semiconductor.[25–29] We use inkjet printing to control the deposition and preparation of dopamelanin and eumelanin-based films and heterostructures. We used optical, structural, and elemental analysis for characterization of melanin nanoparticles and thin films based on melanin and melanin-TiO_2.

Our studies aim, not only to construct melanin-based heterojunctions but to elucidate the unknown photochemical properties of the pigment in pure and heterojunction form. To that end, we integrated steady-state photocatalytic assays with time-resolved spectroscopy. We analyzed pure melanin nanoparticles and melanin nanoparticle-TiO_2 heterostructures under different UV-NIR and Vis-NIR spectral irradiation and observed better photocatalytic characteristics in the heterostructures under the same experimental conditions and both UV-NIR and VIS-NIR irradiation. We have performed ultrafast laser spectroscopy and singular value decomposition to assess the photochemistry of melanin nanoparticles and melanin-based donor-acceptor nanostructured constructs. Our ultrafast laser spectroscopy results show that most of the excited-state absorption (ESA) assigned to the photogenerated charge-carrier absorption relaxes a few picoseconds after excitation. However, ESA and, therefore, charge-carrier absorption last longer in melanin-TiO_2—almost a nanosecond after excitation. These observations indicate charge separation at the melanin-TiO_2 interface and the successful construction of an electronic donor-acceptor structure. The improved photocatalytic characteristics of the melanin-TiO_2 heterostructure in UV-NIR and Vis-NIR, supported by the remarkably long ESA, hold promise for their future wide application in optoelectronic, bioelectronic, and energy-conversion devices.

2. Materials and Methods

Chemical reagents. All chemicals were purchased from Sigma-Aldrich. These main chemicals are used in this study: the dopamine hydrochloride (Sigma-Aldrich), 3,4-dihydroxy-L-phenylalanine (DL-DOPA, Sigma-Aldrich), methylene blue (MB, Sigma-Aldrich), potassium per manganate ($KMnO_4$, Sigma Aldrich), sodium hydroxide (NaOH, Sigma Aldrich), and transparent TiO_2 paste (Sigma-Aldrich, 22 nm particles, > 95% anatase). Deionized (DI) water is used for all synthesis, film fabrications, and all solution preparations.

2.1 Synthesis of melanin nanoparticles

Two chemical types of melanin nanoparticles are made. In one the melanin nanoparticles are formed by spontaneous polymerization of dopamine and we call them dopamelanin. In the second model the chemical oxidation of DOPA has resulted in formation of nanoparticles and we refer to them as eumelanin nanoparticles. The oxidation of DOPA results in generation of oligomers with both 5,6-dihydroxyindole (DHI) and 5,6-dihydroxyindole-2-carboxylic acid (DHICA) units while oxidation of dopamine leads to formation of DHI as the monomer unit. Both DHI and DHICA are known as building blocks of eumelanin family of pigments and therefore both types of synthesized nanoparticle are considered as sub-classes of eumelanin. While the building blocks of dopamelanin and eumelanin nanoparticles are the same, the arrangements of the oligomeric units and the overall polymerization is reported to be different in DHI and DHICA based melanin. DHI units form oligomers with planar structures that are further in the form of highly-stacked graphene-like sheets while DHICA oligomeric structures are non-planar and the polymer is formed by low-stacking degree.[30]

Dopamelanin and eumelanin nanoparticles were synthesized using solution-based and nanochemistry and using previously reported methods.[8,22] The main parameters in obtaining and

controlling the chemical composition and size of melanin are the chemical precursors and their concentration; reaction conditions, such as temperature; and the post-synthesis procedure, as explained below.

Dopamelanin nanoparticles. The dopamelanin nanoparticles are prepared by spontaneous oxidation polymerization of the monomer dopamine. A 50°C solution of dopamine hydrochloride (180 mg) in water (90 ml) is reacted with a 1 M solution of NaOH. Self-polymerization occurs without using any harsh chemicals, and the color changes from pale yellow to dark brown. The reaction continues for 5 hours under vigorous stirring. The steady solution temperature results in nanoparticles of uniform size. In the post-synthesis procedure, immediately after formation, 3-4 consecutive rounds of centrifugation (15-20 minutes at 20000 RPM, Beckman Coulter ultrahigh speed centrifuge) and dispersion in water separate the nanoparticles from the solution. The obtained dopamelanin nanoparticles are well dispersible and stable in water. The concentration of the melanin nanoparticle solution is varied from 1mg/ml to 5 mg/ml.

Eumelanin nanoparticles. The eumelanin nanoparticles are synthesized by chemical oxidation of DOPA. A water-based solution of DL-DOPA (7 M) as starting material is reacted with $KMnO_4$ (1 M). The synthesis reaction is performed at room temperature for 5 hours, and immediately thereafter, the eumelanin nanoparticles are separated from the solution by 3-4 centrifugation cycles (15-20 minutes at 20000 RPM) and redispersion in water at concentrations varying from 1mg/ml to 5 mg/ml. The obtained nanoparticles based solution is stable for several months.

2.2 Synthetic melanin-based heterojunctions

To prepare the melanin-based heterojunction films, we have tried such deposition techniques as simple drop-casting, spin-coating, and a more advanced inkjet printing method.

Preparation of mesoporous TiO_2 film. Before film deposition glass substrates were washed with soapy water and soaked in acetone ultrasonic bath for 15 minutes, followed by sonication in ethanol for the same time and finally rinsed with ethanol. The TiO_2 paste (Sigma-Aldrich, 22 nm particles, > 95% anatase) is used to prepare the TiO_2 films according to the well-characterized method optimized for transparent thin films applied in highly efficient dye-sensitized solar cells.[31,32] The same TiO_2 film is used for studies with and without melanin. A uniform mesoporous film of TiO_2 is deposited on a clean glass substrate by doctor blading of the ink made of TiO_2 nanoparticles. After the paste is deposited, the heat treatment is performed on the film. The TiO_2 pastes are gradually heated under an airflow at 325 °C for 5 minutes, at 375 °C for 5 minutes, at 450 °C for 15 minutes, and finally, at 500 °C for 15 minutes followed by cooling down to room temperature.[25,26] The heating process removes the polymer and leaves the mesoporous film (pore size 21 nm, porosity 65% defined by Brunauer-Emmett-Teller). The thin film is more than 80% transparent in the Vis-NIR region and consists of, more than 95% anatase crystalline phase with optical onset characteristics for anatase TiO_2 (see characterization results).

Drop-casting and spin-coating of melanin nanoparticles. Consecutive layers of melanin nanoparticles are deposited on TiO_2 film in increments of 100 µl at a concentration of 4 mg/ml water. They are allowed to dry for 30 minutes, forming a dense layer over the TiO_2 surface. Drop-casting ink waste is nil or minimal compared to the large waste with spin coating, but the uniformity of the film and the amount deposited are difficult to control (Supplementary Figure S1).

Inkjet printing of melanin nanoparticles. Inkjet printing is practical for thin-film preparation, offering controlled uniform deposition with minimal ink waste. Important considerations for inkjet printing include controlled ink-rheology to obtain a printable ink compatible with the printer in use, chemical and colloidal stability of the ink during the printing process, technical printing parameters, ink-substrate compatibility, and post-treatment process.[33]

Ink formulation. Inkjet printing has been reported for controlled deposition of a variety of nanomaterials and chemicals including silver nanoparticles, graphene nanosheets, and inorganic nanostructures.[33] Surfactants and polymers (such as polyethylene glycol and its similar alternatives, and ethyl cellulose) have been used in the ink formulation. The additive/surfactant can play roles including 1) improving the dispersibility (prevent agglomeration of nanoparticles) and therefore the colloidal stability of the ink, and 2) adjusting the viscosity of the ink which affects the jetting and printability. However, these additional chemical components may affect the actual optoelectronic performance of the as-deposited film and in most cases, a subsequent removal (for example by heat treatment or chemical exchange) of the surfactant or additives is required. Since the target of our study is to study photochemistry and charge carrier processes in the melanin-TiO_2 and melanin films, we avoided the use of additives.

The ink was prepared by centrifugation and dispersion of freshly prepared melanin nanoparticles at different concentrations in water. The size of nanoparticles is controlled by the chemical concentration of the reactant without the need for a surfactant (as is typically used for inorganic nanostructures). The lab-synthesized melanin nanoparticles solution in water after washing and redispersion procedure (see the melanin synthesis method) is stable for several months. A melanin concentration of 500 μg/mL in DI water produced optimal printable ink at pH = 7.33. At this pH, nanoparticle potential is measured at ~ −42 mV using Zeta potential analyzer, and the negatively charged surface makes the ink stable against aggregation without any additional surfactant or stabilizer. The ink was sonicated for three minutes prior to printing for extra caution and to avoid particle aggregation and to prevent nozzle clogging.

Substrate treatment. The most critical task is optimizing the surface energy to control the wettability of the substrate.[33] The surface of the substrate was treated with a plasma cleaner PDC-32G (Harrick Plasma, Ithaca, NY, USA) for about 40 s at medium power, helping the spreading of the ink and formation of homogeneous inkjet-printed films throughout its surface.

Inkjet printing parameters. Melanin nanoparticles are inkjet printed on top of mesoporous TiO_2 film according to a previously reported procedure in which melanin was deposited on glass substrates.[22] The prepared melanin nanoparticle ink was then printed using a piezoelectric inkjet printer (Jetlab IX, Microfab Technologies, Plano, TX, USA) with an 80-μm nozzle. The settings of the printing were established considering parameters such as drop formation, drop satellites, drop volume, drop velocity, throw distance, resolution, and frequency. The voltage was adjusted to have a controlled drop (perfect drop) and to prevent satellites dissociating from the main droplet to form smaller daughter drops that can reduce the thin film's quality. Figure S14 in the supporting information provides a schematic diagram of the printing parameters, and the droplet formation and drop analysis with an example of perfect drop and non-perfect condition. The bipolar waveform (standard wave) is applied to generate the desired droplet for inkjet printing and examples of desired and undesired jetting conditions are shown. The voltage consists of two square wave pulses sequentially positive and negative with a long idle time level. The amount of positive and negative voltages and their difference is used to generate and eject the droplets and the amount depends on the rheological parameters of the ink such as viscosity and is optimized for a given

ink. The dwell time affects the quality of the jetting. In Figure S14b when the dwell time is optimum (30 μs) a perfect droplet is ejected, leading to perfect printing conditions. In Figure S14 c in which the dwell time is other than optimum, the main part of the drop is accompanied by a second droplet (satellite) which has a different speed from the droplet itself. In this case, the main drop and satellite droplet can't merge leading to imperfect printing of thin films. The voltage pulse width is also tuned to obtain the maximum drop volume. Printing parameters were optimized at 9, 30, 5, 30, and 5 μs for rise time 1, dwell time, fall time, echo time, and rise time 2, respectively as it is shown in Figure S14 for the perfect drop. In addition, idle, dwell, and echo voltages were set at 0 V, 34 V, and −30 V. This configuration yielded droplets at 0.35 m/s velocity, 185 pl in volume, and 70.65 μm in diameter (drop analysis shown in Figure S14 for perfect drop).

Post-deposition treatment. The porosity of the TiO_2 film (~60%) allows the printed film to dry quickly. The inkjet-printed films were treated at 60° C for a few minutes to evaporate the solvent. Subsequent printings increase film thickness.

2.3 Thin film and materials characterizations

Zeta potential analyzer (Zetasizer Brookhaven Instrument, Holtsville, NY, USA) was used. An inkjet printer (Jetlab IX, Microfab Technologies, Plano, TX, USA) was employed for film deposition. UV-NIR optical absorption of solutions was measured using an Agilent Technologies Cary 8454 UV-NIR spectrophotometer. A UV-NIR spectrophotometer (Perkin-Elmer Lambda 950) equipped with an integrating sphere (100 mm) is used for total/diffuse transmittance/reflectance spectroscopy measurements of thin films. SEM images were acquired using a high-resolution field emission Zeiss GeminiSEM 300. The FTIR spectrum was measured using a Perkin Elmer Spectrum 100 FT-IR spectrometer equipped with a universal ATR sampling accessory. X-Ray diffraction (XRD) measurements were performed using powder X-Ray diffractometers (D2 and D8, Bruker).

2.4 Photocatalysis experiments

The photocatalysis tests are performed using a photocatalysis and optical spectrophotometry assay previously reported for TiO_2 and other photocatalysts.[25,34,35] For our heterogeneous photocatalysis experiments the sample (melanin/glass, melanin-coated TiO_2 films/glass or reference TiO_2/glass) was immersed in 50 mL of 5 x 10^{-5} M methylene blue solution. The films' area and the amount of material deposited were kept the same across experiments to enable comparison of their photocatalytic properties. The solution was gently stirred. A xenon arc lamp (Oriel, Newport) was used as a UV-NIR light source; its irradiation resembles solar irradiation under A.M. 1.5 conditions (1.5 atmosphere thickness, corresponds to a solar zenith angle =48.2°). In some experiments, a UV filter was applied to cut the wavelengths below 530 nm, and the lamp emitted Visible-NIR light exclusively. To measure the photocatalytic degradation of MB, its UV-NIR absorption spectrum was taken every 30 minutes of irradiation for 180 minutes. Samples are immersed in the solution for 5 minutes before irradiation. An initial recording of MB optical absorption was used as a reference (0-time irradiation). After each illumination period, a sample of about 2 ml of the MB solution is collected and transferred to a cuvette. The UV-NIR absorption spectrum of the MB sample in the cuvette is obtained. After measuring the absorption, the MB solution is added back to the initial photocatalysis test beaker with care. The whole steps are done carefully so that the volume of the MB remains constant during the experiment. The degradation of MB is evaluated according to equation (1) in which the C_i and C_t are respectively the initial concentration and concentration of MB at time t. The A_i and A_t are the initial optical absorption of

MB solution (at absorption peak at 650 nm) and optical absorption of MB solution after irradiation time t. For a transparent solution, the optical absorption and concentration are related via the Lambert-Beer law.

$$Relative\ MB\ concentration\ (t)\ = \frac{C_t}{C_i} = \frac{A_t}{A_i} \quad (1)$$

2.5 Pump-probe laser spectroscopy measurements

The ultrafast pump-probe transient absorption spectroscopy (TAS) technique uses femtosecond pulses provided by a PHAROS laser (20 W, 1030 nm, Light conversion) operating at 100 kHz. The pump at different wavelengths relies on an optical parametric amplifier (ORPHEUS) in tandem with a harmonic generator (LYRA). The excitation is provided by the pump beam at 460 nm. The probe beam is a white-light continuum generated in a sapphire plate that has less energy than the pump on the sample to avoid multiple excitations. Pump and probe pulses length is ~ 220 fs and the time-resolution of measurements is about 350 fs (overlap time of pump and probe). The pump and probe pulses have a repetition rate of 100 kHz with the pump modulated before the sample for $pump_{on}$ $pump_{off}$ measurements. The effective acquisition rate is typically 3 KHz, and a few thousand spectra are averaged for each spectrum. The typical probe power is 400-800 μW and pump power is typically 0.1-1 mW at the sample. The broadband spectrum is acquired using a spectrograph-equipped Si photodiode array (Andor Kymera). The overlap time of pump and probe is wavelength dependent due to the chirp of the white light. We have used a standard procedure for chirp correction (as explained below). The chirp is corrected by fitting the temporal responses with the cross-correlation function between the pump and supercontinuum probe and its derivative to access the correct time-delay response for different wavelengths.

The samples were translated during measurements to eliminate overexposure and chromophore instability. This also provides the possibility to measure different spots on the sample testing its homogeneity. Alternatively, control tests can be done without moving the sample to check the TAS signal after consecutive measurements on the same spot on the sample. In control experiments, measurements were performed at different points of the sample and the amplitude of the TAS signal and decay traces were compared. If the pump power is not too high (which is the case for all real measurements reported in this study) the signal (amplitude and kinetics) is reproduced in consecutive measurements. Graphs are made using Phyton, MATLAB, or Igor Pro software.

3. Results

3.1 Structural and optical characterization of synthetic melanin nanoparticles

SEM analysis of the synthesized melanin (Figures 1a, b) shows nanoparticles of uniform size. The eumelanin and dopamelanin nanoparticles are well separated, and we observe no aggregates and size inhomogeneity as is often the case with synthetic melanin and melanin pigments extracted from biological sources. The average size of dopamelanin nanoparticles and eumelanin nanoparticles is 160 nm and 100 nm respectively (size distribution is provided in Supplementary Figure S13). Figure 1c provides an example of the evolution of optical absorption of the dopamelanin solution during the synthesis. The dopamine precursor absorbs UV. A few minutes after introducing the oxidizing agent and initiation of oxidation/oligomerization the absorption onset redshift and another peak appears at 430 nm. Further continuation of the reaction results in the broad absorption spectrum extended to visible and NIR regions. The UV-Vis absorption spectra of the eumelanin and dopamelanin solution are characterized by the typical featureless

broadband UV-NIR absorption (Figure 1d). The concentration of both eumelanin and dopamelanin solutions is 1 mg/ml. The XRD of eumelanin shows a single broad peak around 25° that can be assigned to an amorphous structure (Figure 1e). Previous reports also assigned it to the interlayer spacing of the melanin stacked sheets.[36] According to the Bragg equation:

$$2dsin\theta = n\lambda \quad (2)$$

where θ represents the diffraction angle; n is the diffraction order; and λ is the X-ray wavelength, or 1.5406 Å for the CuK_α X-ray irradiation source. Considering first-order diffraction (n=1), we obtain d =3.5 Å for eumelanin. This spacing is in strong agreement with the literature value for interlayer spacing in the noncovalent heteroaromatic π-π stacked sheets model proposed for eumelanin extracted from sepia-officinal observed by AFM microscopy, and synthetic eumelanin observed by HRTEM.[36,37] ATR-FTIR analysis of synthetic melanin nanoparticles (Figures 1f,g) shows the characteristic IR-absorption features for eumelanin and dopamelanin in agreement with previously observed in fossil, melanin from Sepia Officinalis (natural eumelanin extracted from the ink sac of cuttlefish), and other natural melanin sources.[38–40] The broad absorption around 3100 cm^{-1} can be due to associated or polymeric OH hydroxy groups, and N-H and O-H stretching in carboxylic acid. The absorption around 2800 cm^{-1} belongs to C-H stretching. The fingerprint regions between 700 cm^{-1} and 1500 cm^{-1} resemble those previous reports for eumelanin and dopamelanin due to bending vibration modes of aromatic ring C=C and C=N bonds, aliphatic C-H groups, and OH bending of phenolic and carboxylic groups.[38–40]

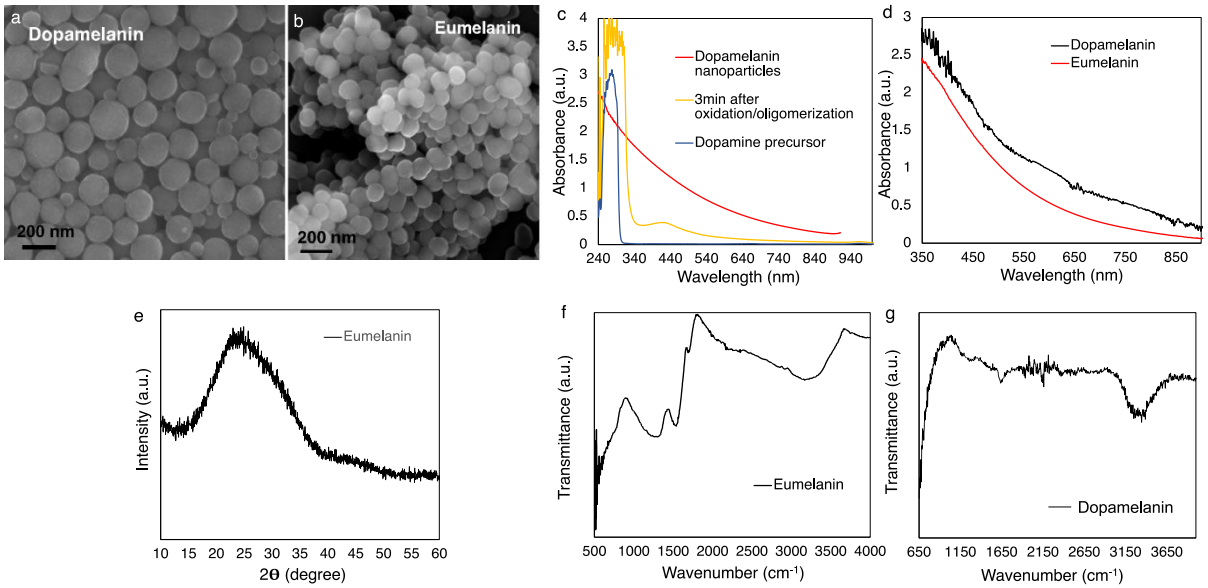

Figure 1. Optical and structural characterization of synthetic melanin nanoparticles. a,b) SEM images of dopamelanin and eumelanin nanoparticles showing the uniform size and spherical shape with average diameters of 170 nm and 110 nm respectively. Particles are well separated, and no clusters and aggregates are observed. c) Optical absorption spectrum of dopamelanin synthesis reaction at initial steps; the dopamine hydrochloride precursor absorbs in UV with an edge at 309 nm. The optical absorption of the solution at 3 minutes after the addition of NaOH (start of the oxidation and oligomerization) shows the absorption shoulder is red-shifted, and a peak appears at 430 nm. d) The UV-Vis optical absorption spectrum of dopamelanin and eumelanin nanoparticles. The concentration of both solutions is 1 mg/ml. The optical spectrum is characterized by a broad,

featureless absorption from UV to NIR. d) XRD analysis of eumelanin nanoparticles showing a broad peak assigned to diffraction from 3.5-Å spacing of the noncovalent π-π stacked heteroaromatic sheets. e,f) ATR-FTIR spectra of synthetic eumelanin and dopamelanin nanoparticles.

3.2 Structural and optical characterization of melanin-TiO_2 based heterostructures

Figure 2 shows the structural characterization of printed melanin-TiO_2 film. Figure 2a is a schematic of the inkjet printing method; optimized printing conditions and optimized ink deposit a uniformly dense film of melanin on the mesoporous film. Panel b presents images of the TiO_2 film before the removal of the polymer and after melanin deposition. SEM analysis of the melanin-TiO_2 film (Figure 2c) confirms uniform coating across a large area. The SEM image of mesoporous TiO_2 film shown in Supplementary Figure S2 identifies the size of the particles as 20-40 nm, with the pore size in the same range. As a result, the 120-200-nm melanin particles cannot infiltrate the pores of the TiO_2 film and form a film on top (bilayer structure). The thickness of the TiO_2 film after heat treatment and removal of the polymer is 1.2 μm, and AFM and a surface optical profilometer identified a ~300-nm melanin layer deposited on the TiO_2 after one printing. UV-Vis (Figure 2d) shows that successive depositions of melanin to increase film thickness improves optical absorption in the entire UV-NIR region (see also Figure 3). Figure 2e shows the XRD results for eumelanin, TiO_2 mesoporous film, and eumelanin-TiO_2-based films. The sharp crystalline peaks of TiO_2 show that the main crystalline phase is anatase (>95%) with some minor contribution from rutile TiO_2. The XRD pattern of TiO_2 crystals in the two samples of dopamelanin-TiO2 and eumelanin-TiO_2 is identical as the same TiO_2 film is used. The melanin crystalline peak is much broader. It may indicate small domains of π-stacked planar moieties; their overall position makes the polymer amorphous.

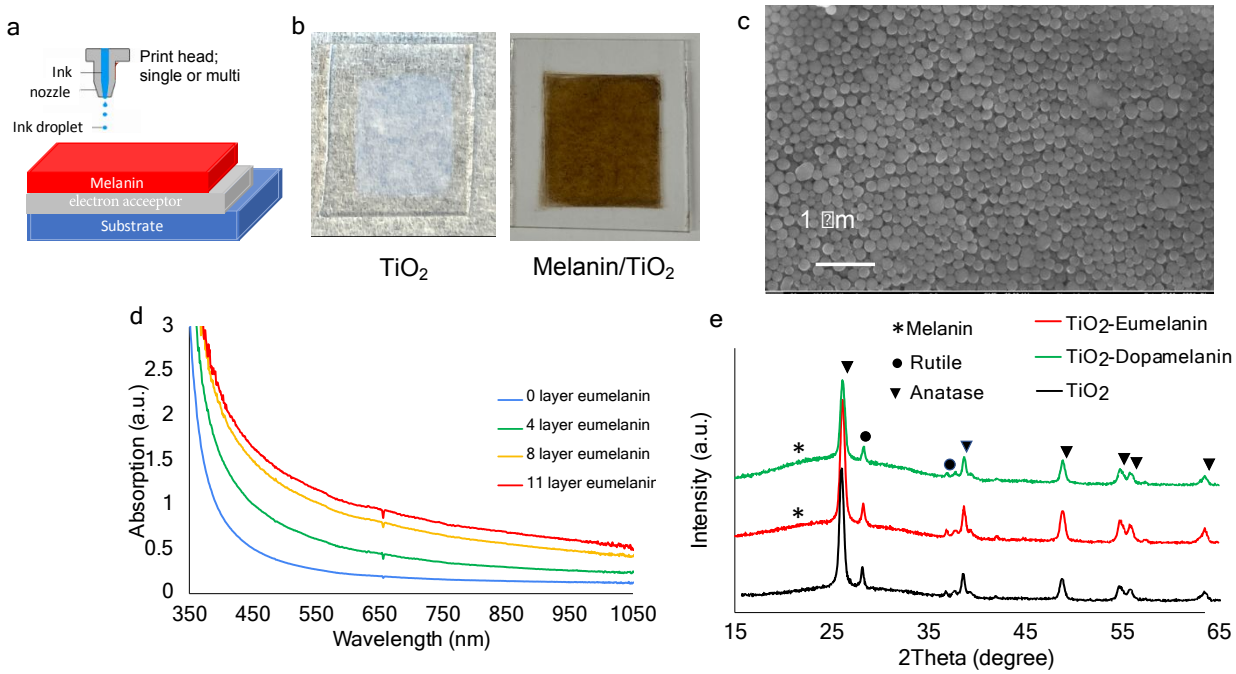

Figure 2. Optical and structural characterization of the printed synthetic melanin/TiO_2 nanoparticle-based films. a) Schematic of inkjet printing of the melanin nanoparticle-based

heterostructure. Successive printing deposits single layers of melanin nanoparticles on TiO_2 mesoporous films. b) A typical optical micrograph of transparent TiO_2 film prepared by doctor blading (after heat treatment), and after deposition of 11 uniform, ultimately dark brown melanin layers. c) SEM of dopamelanin film. d) UV-NIR optical absorption spectrum of melanin-deposited TiO_2 film. Successive deposition improves optical absorption in the entire UV-NIR region. (e) XRD spectrum of pure TiO_2 film, eumelanin-TiO_2 film, and dopamelanin-TiO_2 film. XRD of TiO_2 identifies that most of it is anatase phase, with some rutile contribution. The broad pattern in eumelanin-TiO_2 and dopamelanin-TiO_2 is attributed to the broad spectrum of melanin.

Figure 3 shows the optical analysis of the eumelanin-TiO_2 (the same sample condition for which the photocatalysis and laser spectroscopy experiments are reported) and TiO_2 films. The total transmittance (direct transmittance and diffuse transmittance), diffuse transmittance, total reflectance (specular and diffuse reflectance), and diffuse reflectance of the samples are measured using an integrating sphere-equipped UV-NIR spectrophotometer.

The total absorptance (A) of the films which represents the fraction of light that is absorbed considering the losses by total reflected and total transmitted light is calculated using equations 3-5.

$$A\ (\%) = 100 - Ttotal - Rtotal \quad (3)$$

$$\mathrm{R\ total} = \mathrm{Rdiffuse} + \mathrm{Rspecular} \quad (4)$$

$$\mathrm{T\ total} = \mathrm{Tdiffuse} + \mathrm{Tdirect} \quad (5)$$

In Figure 3a the absorptance of the eumelanin-TiO_2 samples with different numbers of eumelanin coatings and TiO_2 samples is provided. The characteristic sharp absorption edge of TiO_2 film at 380 nm is observed for the TiO_2 sample. For the melanin (3 layers)-TiO_2 sample, an improved absorptance in the UV-NIR region is observed. The shape of the absorptance spectrum resembles the exponential trend of melanin with a larger absorption increase in the blue region compared to the red region (also see the exponential trend of melanin absorption in Figure 1d). These results are particularly important for the comparison of the photocatalytic characteristics of the film by comparing the fraction of absorbed light. By increasing the number of coatings, the absorptance spectrum further increases in the UV-NIR region. For example, at 550 nm the absorptance of TiO_2 is less than 8 % and increases to 20% and 60% by deposition of 3 and 12 layers of eumelanin respectively. In Figures 3b-3d the total and diffuse optical components measured in transmission and reflection for each sample are provided. For all samples, the values of R_{total} and $R_{diffuse}$ are close to each other, and both are smaller than 20% indicating that the specular reflection and back-scattering are not considerable (scattering is negligible in the backward direction). The $T_{diffuse}$ is also much smaller than T_{total} which again confirms that most of the light is transmitted directly and not through scattering events (scattering is negligible in the forward direction). The optical characteristics of dopamelanin (2 layers)-TiO_2 film is also provided in supplementary information Figure S16 and the same trend is observed for dopamelanin-based films. Therefore, the diffuse scattering measurements in transmission and reflectance modes confirm that the scattering processes are not dominant.

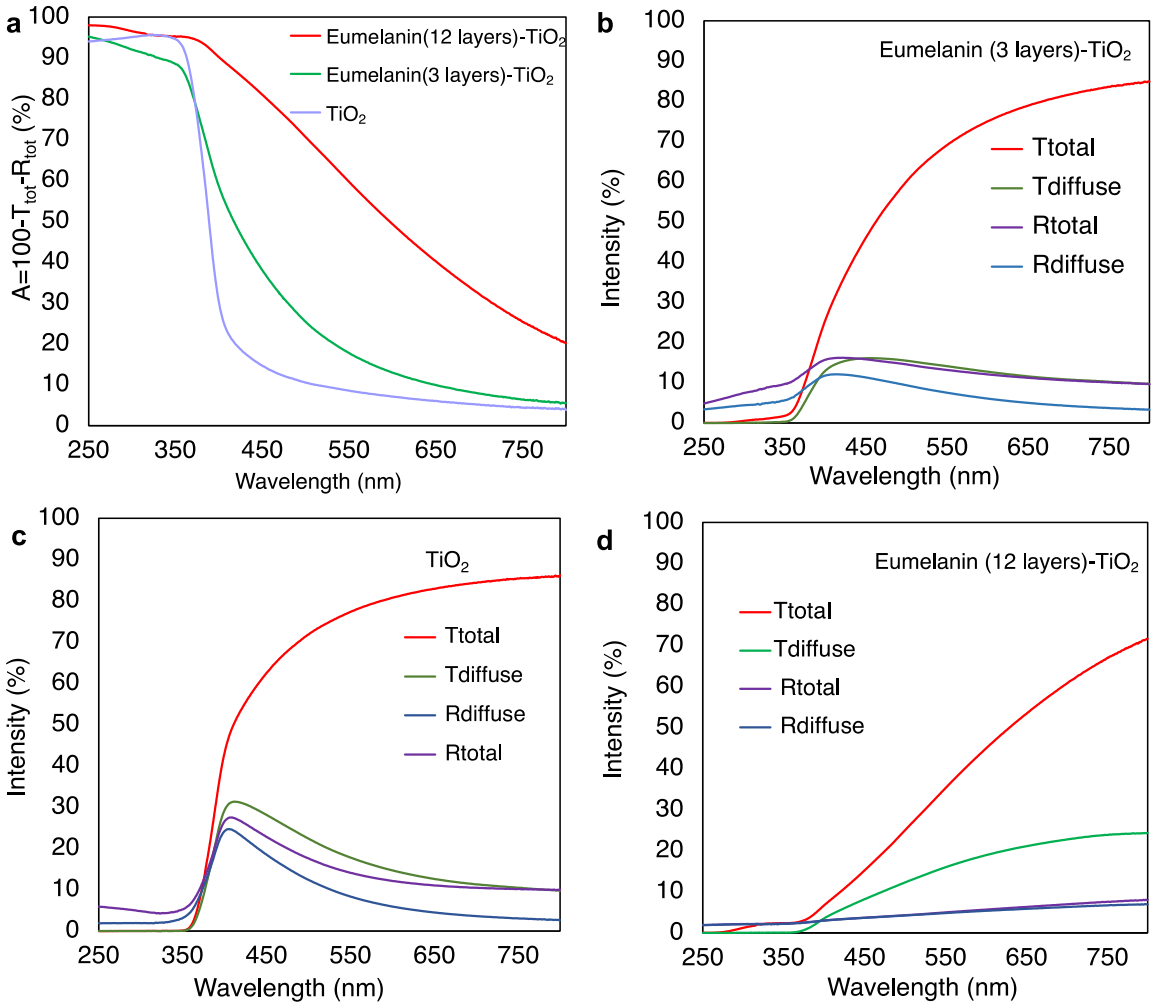

Figure 3: Optical characterization of eumelanin-TiO_2 and TiO_2 films. a) The absorptance of eumelanin-TiO_2 samples with different numbers of coatings is compared with that of TiO_2. Eumelanin deposition has resulted in enhanced absorptance in the entire UV-NIR with an exponential trend typical of the absorptance spectrum of melanin. b-d) The total transmittance, diffuse transmittance, total reflectance, and diffuse reflectance of the three samples are shown. For reflectance mode measurements, there is almost no specular reflectance, and the diffuse reflectance is much less than 20%. In transmission mode, the diffuse transmittance of the film is much smaller than the total transmittance. Measurements in both transmittance and reflectance modes indicate that the light scattering process is not dominant in the films. Consecutive deposition of melanin increases the absorptance of the film.

3.3 Photocatalysis characteristics exploring the photochemistry of melanin-TiO_2 molecular junctions

Not to find an optimal photocatalyst, but rather to investigate and compare the photochemical characteristics of the synthesized melanin nanoparticles and melanin-TiO_2 nanostructures, we tested the photocatalytic degradation of methylene blue under Vis-NIR (λ>530 nm) and UV-NIR irradiation conditions provided by a xenon lamp at A.M. 1.5. We compared different melanin types, including dopamelanin, eumelanin, and melanin-TiO_2 heterostructures, using the pure

melanin films and TiO_2 films as references. For all photocatalysis tests solid samples (photocatalyst deposited on glass substrate) are used and soaked in MB solution (for details see the photocatalysis experimental procedure).

Photocatalytic properties of dopamelanin nanoparticles-TiO_2 nanostructures under UV and visible light irradiation. The results of photocatalysis experiments using dopamelanin-based samples are provided in Figure 4. Figure 4a, shows the absorption spectrum of MB and the decrease in the amplitude of its two characteristics peak upon UV-NIR irradiation. The decay of MB absorption peaks represents the photocatalytic degradation of MB using dopamelanin-TiO_2 thin films under UV-NIR illumination. In Figure 4b, the MB degradation is compared for melanin-TiO_2 and TiO_2 samples obtained using equation 1 under the same experimental conditions and with UV-NIR irradiation; Supplementary Figures S4 and S5 show details of experiments. More than 90% of the MB is degraded after 180 minutes of irradiation on both samples, yet remarkably, especially since TiO_2 is known as an efficient and standard photocatalyst, the photocatalytic performance of the dopamelanin-TiO_2 nanostructure is comparable to that of TiO_2 film. In Figure 4c, the photocatalysis experiments under Vis-NIR irradiation are compared for different samples; dopamelanin-TiO_2 film, pristine dopamelanin nanoparticles-based film, and TiO_2 film as the control sample. It should be noted that the same amount of dopamelanin (3 layers) was deposited on glass and TiO_2 to ensure a fair quantified comparison. No photocatalytic activity is observed for TiO_2 film under Vis-NIR irradiation as expected since TiO_2 only absorbs wavelengths below 380 nm (Figure 3a). The dopamelanin film shows more photocatalytic activity than TiO_2 which can be related to its increased optical absorptance in Vis-NIR. Interestingly, by deposition of the same amount of melanin on TiO_2 film the photocatalysis activity further increases and the dopamelanin-TiO_2 film shows the most photocatalytic activity. The optical absorptance of dopamelanin-TiO_2 film (Figure S16) shows that the diffuse reflectance of the film is less than 10%. The Absorptance of the film increases from ~10% at 890 nm to ~55% at 440 nm with a further enhancement at shorter wavelengths (bandgap of TiO_2 and absorption by dopamelanin building blocks). The whole activity of melanin-TiO_2 in the visible-NIR region is remarkably less than that in UV-NIR, which can be explained by the stronger absorption power in the UV region.

Several control tests are performed to examine several additional processes that can potentially affect the experiments including the effect of physisorption (MB physical adsorption on the surface of photocatalyst), conducting experiments under dark, and MB degradation upon irradiation in the absence of any photocatalyst (results are provided in Supplementary information). As an example, the optical absorption spectrum of the dopamelanin-TiO_2 sample before and after photocatalysis experiments is provided in Supplementary Figure S6. A small peak that belongs to MB shows the amount of absorbed MB, but its small amplitude confirms that the amount of MB adsorbed on the surface of the photocatalyst after the experiment is negligible compared to the observed actual change in the optical absorption of MB solution by photocatalysis experiment. Note that after the photocatalytic experiments, the melanin sample is robust: with no damage or degradation as Figure S6 shows. Control tests under dark conditions showed no MB degradation (Figures S7 and S8). All the experiments shown in Figure 4 and control tests conclude that the absorption changes of MB reflect the photocatalytic degradation due to the photocatalytic reaction. Since TiO_2 is not active in Vis-NIR, and the same amount of melanin is present in melanin and melanin-TiO_2 samples, the improved photoactivity observed for melanin-TiO_2 is primary evidence of interfacial charge separation at the molecular junction of melanin and TiO_2.

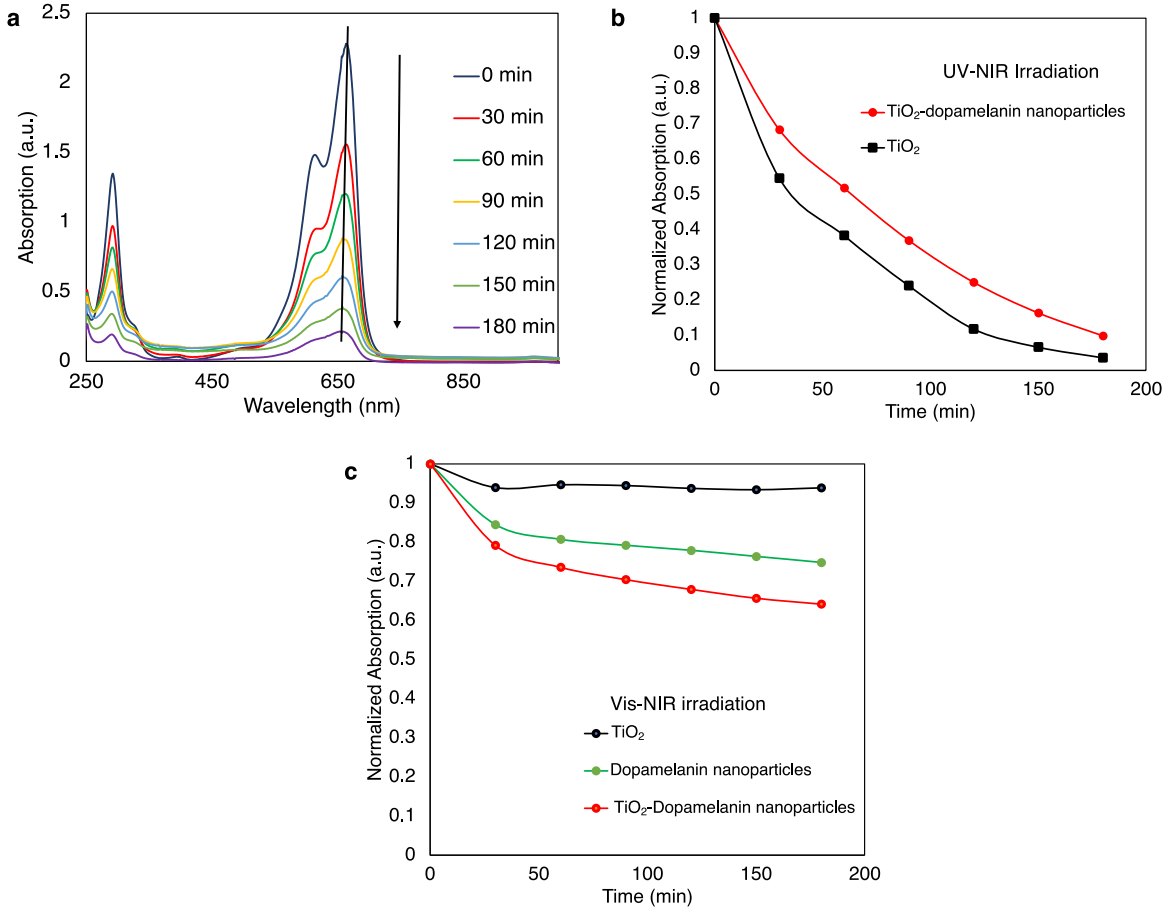

Figure 4. Photochemical analysis of dopamelanin and dopamelanin-TiO_2 heterostructures. Photocatalytic decomposition of methylene blue using dopamelanin nanoparticles and dopamelanin-sensitized TiO_2 thin films. a) The time-evolution of the optical absorption spectrum of MB solution after photocatalytic reactions using dopamelanin-TiO_2 under UV-NIR irradiation conditions. The decay of the absorption peak at 650 nm reflects the photocatalytic degradation of MB. b) Photocatalytic degradation of MB using dopamelanin-TiO_2 and pure TiO_2 films under UV-NIR. Remarkably, the photocatalytic performance of the dopamelanin-TiO_2 nanostructure is comparable to that of TiO_2 film, the standard, highly efficient photocatalyst. c) Photocatalytic degradation of MB using dopamelanin-TiO_2 sample and dopamelanin-glass sample (the amount of dopamelanin is the same in both samples), and the reference pure TiO_2-glass, under Vis-NIR irradiation (UV is blocked). The improved photoactivity, in melanin-TiO_2, is primary evidence of interfacial charge separation at the molecular junction of melanin and TiO_2.

Photocatalytic properties of eumelanin nanoparticles and eumelanin-TiO_2 donor-acceptor heterojunctions under UV-NIR and Vis-NIR light irradiation. Figure 5 shows the photocatalytic properties of the eumelanin-based thin films and eumelanin-TiO_2 donor-acceptor structures under two illumination conditions, UV-NIR and Vis-NIR. To compare their performance, we kept the macroscopic surface area the same. Three consecutive deposits of eumelanin ensured that the entire surface of the TiO_2 film was covered, forming a bilayer melanin-TiO_2 structure.

Several striking differences can be observed in Figure 5. First, the photocatalytic decomposition rate of MB for the eumelanin thin films under Vis-NIR illumination is negligible. Anchoring the same amount of eumelanin to the surface of the TiO_2 film improves it. Second, the photocatalytic performance of both eumelanin-TiO_2 and eumelanin nanoparticle thin films improved under UV-NIR irradiation due to the materials' increased absorption in the UV region. Third, for both UV-NIR and Vis-NIR irradiation conditions, the photocatalytic performance of the eumelanin-TiO_2 film is better than that of eumelanin alone. TiO_2 can only be active in the UV part (as Figure 3, and photocatalysis tests in Supplementary Figures S 4b and S 5b confirm), and the TiO_2 substrate cannot actively participate in the photocatalytic degradation reaction because its surface is covered with a dense melanin layer. Therefore, the improved photocatalytic performance of eumelanin-TiO_2 compared to melanin in both irradiation regions strongly suggests that the interfacial charge separation is responsible for efficient MB degradation.

In Figure 5c, the photocatalysis tests on eumelanin (12 layers)-TiO_2 is provided. Increasing the amount of eumelanin-TiO_2 sample from 3 to 12 layers improved its photocatalytic activity but not linearly. The optical characteristics of the films including the absorptance spectra are provided in Figure 3. At 550 nm the absorptance of TiO_2 is less than 8 %, and it is increased to 20% and 60% by deposition of 3 and 12 layers of melanin respectively. At 650 nm, the absorptance of the melanin-TiO_2 film is 12% and 40% for 3 layers and 12 layers of eumelanin coatings respectively. In the Vis-NIR region, the absorptance of the film is increased by approximately 3 times. The photocatalytic degradation is improved by 1.4 times. Two processes play a role here: the melanin's optical absorption power is increased, and the TiO_2 junction's influence on charge separation is negated. While the scope of this work is not to optimize a photocatalyst, we expect a bulk-heterojunction morphology would be stronger than the bi-layer structures under study.

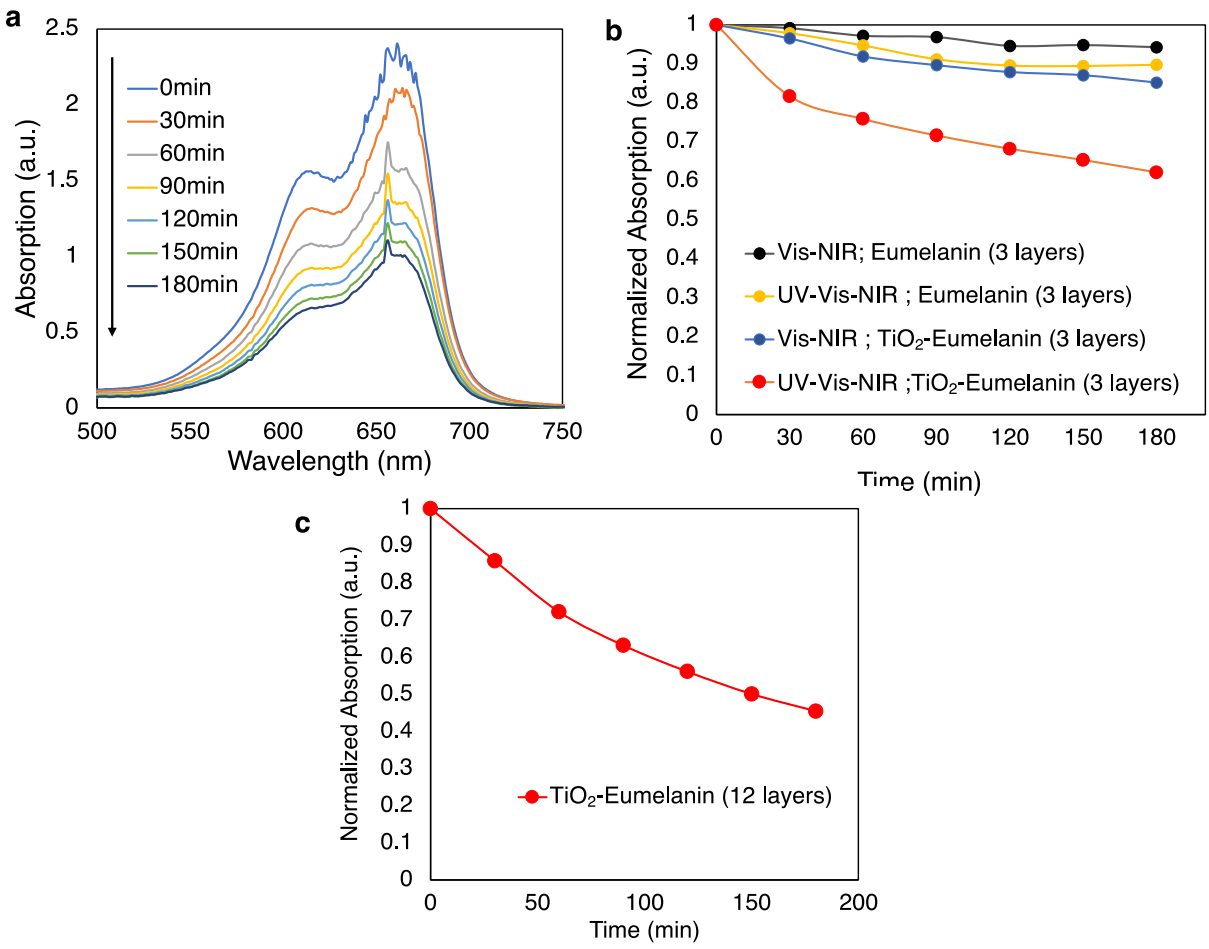

Figure 5. Photoactivity of eumelanin-TiO_2 nanoparticles. a) The time-evolution of the optical absorption spectrum of MB solution as a result of photocatalytic reactions by eumelanin (12 layers)-TiO_2 under UV-NIR irradiation conditions. b) The kinetic comparison of MB degradation using eumelanin and eumelanin (3 layers)-TiO_2 samples under Vis-NIR and UV-NIR irradiation. In the Vis-NIR, the photocatalytic performance of the eumelanin film is minimal; it improves under UV-NIR irradiation. Eumelanin (3 layers)-TiO_2 sample shows enhanced photocatalytic performance remarkably under both UV-NIR and Vis-NIR irradiation. c) Photocatalytic activity of eumelanin (12 layers)-TiO_2 sample. By increasing the number of eumelanin-deposited layers, the photocatalytic activity is further improved.

3.4 Ultrafast transient absorption spectroscopy of melanin nanoparticles and melanin-TiO_2

Ultrafast pump-probe transient absorption spectroscopy experiments were carried out on films made of synthetic melanin nanoparticles and eumelanin nanoparticles (12 layers)-TiO_2 prepared under the same conditions used in optical characterization and photocatalysis experiments. Samples were excited at 460 nm to affect melanin but not TiO_2. The probe is a white-light supercontinuum detected in the 500-950 nm spectral range. The time resolution of the TAS experiments is 330 fs defined by the temporal broadening of the pump and probe and their overlap time. Figure 6 shows the TAS spectrum for probe wavelengths ranging from 500 nm-950 nm and

from a negative delay (when the probe arrives before the pump) to a positive delay close to 1 ns (the probe arrives after the pump). Pump power is typically 460 μW (see experimental procedure for details).

Figure 6a shows the broadband TAS spectra and 6b the time-resolved TAS kinetics of melanin nanoparticles until 70 ps. The 70 ps-short scan time traces are shown in Figure 6b to emphasize the ultrafast dynamics within this time scale. The long-scan time traces until 795 ps are also provided in supplementary Figure S12. Figures 5 c,d represent the same measurements for melanin-TiO_2; note that the shapes of their TAS spectra differ (Figures 6 a,c). The melanin sample shows a negative signal in the 530-600 nm spectral region and a positive signal at the longer wavelengths. The negative peak may result from a combination of ground-state bleaching (GSB), when charge carriers are localized in electronic states, and radiative recombination arising from such states. The spectral location of the negative peak is in agreement with our previous report in which we observed an excitation wavelength-dependent photoluminescence using non-time-resolved confocal photoluminescence imaging.[22] The positive and negative signals relax and the negative peak blue shift and change sign, suggesting that in the 500 nm-600 nm spectral region, ESA and GSB overlap, and with bleach recovery, ESA reappears. In the spectral region above 650nm, ESA relaxes over time; for melanin, in less than 20 ps. The normalized long time-delay TAS kinetics of the excited state relaxation recorded at different wavelengths in the 600 nm-920 nm spectral region is also provided in Figure S9. The normalized short time-delay TAS signals at different probe are also provided in the inset of Figure 6b (and an enraged graph in supplementary Figure S10). The time-traces at 707 nm and 920 nm are fitted with double exponential decay functions. The y0 is the signal residual, A is the pre-exponential factor, and τ is the time constant (see Equation S1 in supplementary information). The fitting parameters for 920 nm-probe are A1 = 0.168, τ1 = 5.99 ps, A2 = 0.730, τ2 = 0.239 ps and y0= 0.05, and for 707 nm-probe are A1 = 0.065, τ1 = 1.9 ps, A2 = 1.94, τ2 = 0.135 ps and y0= 0.024. The τ2 values are within the time-resolution of the TAS experiment (350 fs). The τ1 values reflect the ESA relaxation time constant of melanin being 5.99 ps and 1.9 ps recorded at 920 nm and 707 nm. The ESA decay is slightly slower further in the infrared region. This can be also understood in terms of less spectral overlap of ESA and GSB in the 800-919 nm region compared to the 611 nm and the kinetic in the former region can reflect the pure contribution of ESA. In either region, the majority of the signal decays in less than 10 ps. The ultrafast ESA relaxation in this study using the broadband TAS spectroscopy and 460 nm-pump (pump and probe pulses at 100 KHz) agrees with previous report on TAS spectroscopy of melanin using two-color pump-probe using 720 nm-pump and 817 nm probe (at 2 MHz) in which a sub-10 ps relaxation was reported.[41] TAS spectrum for melanin-TiO_2 (Figure 6c) shows positive ESA and it relaxes at about 400 ps (Figure 6d). Figure S10 shows the normalized excited-state relaxation kinetics of melanin-TiO_2 at different wavelengths. About 95% of the signal decays 100 ps after excitation and the remaining 5% over 1 ns. The time-delayed TAS signals are fitted with double exponential decay function and the result is provided in supplementary Figure S18. The fitting parameters for 920 nm-probe are A1 = 0.19263, τ1 = 36.3 ps, A2 = 0.75663, τ2 = 1.28 ps and y0= 0.15428. The fitting parameters for 717 nm-probe are A1 = 0.23881, τ1 = 23.44 ps, A2 = 0.72454, τ2 = 0.968 ps and y0= 0.10804. The fit parameters for 548 nm-probe are A1 = 0.28886, τ1 = 15.94 ps, A2 = 0.74, τ2 = 0.818 ps and y0= 0.063429. For melanin-TiO_2 sample, at each probe wavelength, both τ1 and τ2 time constants are bigger compared to those for melanin sample. Figure S11 shows the TAS spectrum of the TiO_2 reference sample. The experimental conditions are similar to those for the melanin and melanin-TiO_2 samples. No transient absorption signal is observed at 460 nm excitation, as expected: TiO_2 does

not absorb the pump beam (supplementary Figure S11). The absorption edge of TiO_2 is at 380 nm and the absorptance of the beam at the pump wavelength is less than 12%. The absorptance of melanin-TiO_2 sample at 460 nm is increased to 80% and 35% by 12 layers and 3 layers of melanin respectively. Our control studies show that if the TiO_2 film is excited at higher powers (above 3 mW), the contribution from direct excitation within sub-bandgap states in TiO_2 appears. The high repletion rate of our measurements enables measurements at low power excitations with reasonable signal to noise as Figure 6 shows. Also, the presence of a highly absorbing melanin layer on top will screen the excitation to reach the TiO_2 layer underneath. Therefore, under the conducted experimental condition-excitation at 460 nm and low power regime (460 μW pump power), direct excitation of melanin and the observed TAS signal in melanin and melanin-TiO_2 reflect photoabsorption by charge carriers generated in melanin. The longer ESA and GSB relaxation time in melanin-TiO_2 points to longer-lived charge carriers as a result of interfacial charge separation between melanin and TiO_2. Note that, as the initial photoexcitation (charge carrier formation) occurs in melanin (due to the excitation spectral region) the longer-lived photo excitation is evidence for electronic interactions between melanin and TiO_2; namely interfacial charge separation (photosensitization). We have previously shown that photoinjected electrons from organic or metal-organic dyes into TiO_2 are stable for long times of milliseconds after injection.[29,32]

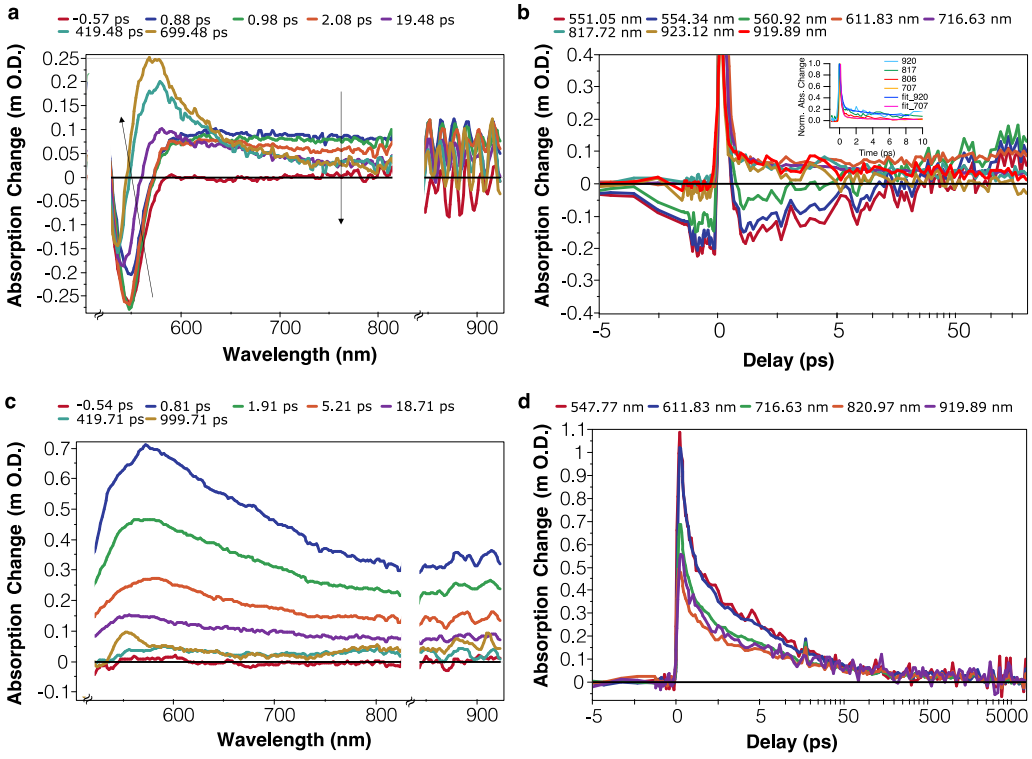

Figure 6. Pump-probe transient absorption of melanin nanoparticle and melanin-TiO_2 films. Samples are excited at 460 nm. The broadband transient absorption spectrum (TAS) is measured in the 500 nm-950 nm spectral region. a) Broadband TAS spectra and b) TAS time-traces at different probe wavelengths for the melanin sample; The inset shows the normalized short time delay-TAS signal until 10 ps at different probe wavelengths in NIR region. The magenta and blue traces are the double-exponential fit to the TAS at 707 nm and 920 nm respectively. The τ1

= 1.9 ps and τ1 = 5.99 ps respectively for 707 nm and 920 nm, τ2 = 0.135 ps and τ2 = 0.239 ps for 707 nm and 920 nm respectively (both τ2 are within the time resolution~350 fs), c) broadband TAS spectra and d) TAS time-traces at different probe wavelengths for the melanin-TiO_2 film sample. Remarkably, the shapes of the broadband spectrum and time evolutions differ completely. TAS decay for melanin is 10 ps, but 400 ps for melanin-TiO_2.

The results provided in this study are the summary of many experiments and sanity checks in different conditions. The samples were mounted on an automatic translation stage which provides the possibility to move the sample gently during the measurement. Linear or random walk scans can be performed. Scans in both moving and fixed conditions led to identical results. An example control test at much higher power (compared to what is reported in Figure 6) is presented in supporting Figure S15. Two consecutive TAS measurements on the same spot on the sample and under identical condition is provided in panels and b. The samples are excited at 460 nm with 5.5 mW pulse energy. The WL probe power is 558 μW. The amplitude of the TAS signal and decay kinetics is reproduced. Note that the experiments shown in Figure 6 are performed at much lower power (pump 460 μW).

3.5 Singular value decomposition analysis

SVD is a mathematical method used to analyze spectroscopic data.[42,43] The outcome of time-resolved TAS measurements is a rectangular (m × n) matrix in which the values represent the spectral- and time-dependent absorption change of the probe (ΔOD) due to pump excitation. Equation 6 factorizes it as:

$$\Delta OD = A = U.S.V^T \quad (6)$$

where U and V are orthonormal vectors representing the left and right singular vectors, respectively. U is an (m × m) complex and unitary matrix ($U^TU = I_{m\times m}$). Its columns are the orthonormal eigenvectors of AA^T and represent the left singular vectors (gene coefficient vectors). S, with the same dimensions as ΔOD=A, is an (m × n) rectangular diagonal matrix of the singular values, with nonnegative real numbers on the diagonal. The main diagonal values of this matrix are the square roots of the eigenvalues of A^TA. V^T is a transpose of an (n × n) matrix. Its columns ($V^TV = I_{n\times n}$) contain the orthonormal eigenvectors of A^TA, and its rows are the right singular vectors (expression-level vectors).

The data matrix A is best approximated in a least-squares sense by matrix A′, which derives from the most significant (components); significant columns of U, diagonal elements of S, and rows of V^T (U′, S′, and V'^T in equation 7).

$$A \approx A' = U'.S'.V'^T \quad (7)$$

The other components decay exponentially according to the scree plot of eigenvalues and are dominated by random noise or other error sources. Therefore, SVD acts as a noise filter, separating the signal in the first few significant components from the noise in the remaining insignificant singular vectors, which are omitted from the reconstruction.

Figure 7 shows the SVD results for the melanin and melanin-TiO_2 samples, including the three main components and their eigenvalues. The scree plots of the SVD analysis including the eigenvalues for the three significant principal components and the other non-significant components are provided in the supplementary Figure S17. Figure 7a identifies the spectral contribution of excited-state absorption, ground-state bleaching, and instantaneous signal at the

pump-probe overlap time for the melanin sample. The time-evolution of these components is shown in the temporal graph. Figure 7b identifies the excited state absorption, the ground state bleaching, and again an instantaneous signal. The instantaneous signal appears at the pump-probe overlap time and is assigned to optical processes such as self- or cross-phase modulation which is not the interest of our discussion. The red trace in spectral components of both melanin and melanin-TiO_2 samples reflects the excited state absorption and is extended from 520 nm to 930 nm. The ESA component shape is almost the same in both samples, which is expected as the primary photoexcitation is in melanin. For the melanin sample in the 520 nm-650 nm, there is a spectral overlap of different components: intense GSB (blue curve) and ESA. In the TAS result also a signal sign change in this region is resolved. Another weak GSB-type component is resolved above 580 nm (green curve) which is less significant than the GSB in 520 nm-600 nm according to their eigenvalue magnitude (13.9 for blue and 5.7 for green trace in melanin spectral component). The time evolution of these components is provided in the temporal vector data. For the melanin-TiO_2 sample in Figure 7b, in the 520 nm-600 nm, the GSB bleach component (blue trace) is much less significant than that in melanin. The green broad and bleaching component above 580 nm (green curve) is observed. Both bleaching components are less significant in the TAS signal in melanin-TiO_2 compared to melanin (6.3 for blue and 3.8 for green in the melanin-TiO_2 spectral component)

In the spectral component data of melanin sample (Figure 7a), an intense GSB-type component is resolved in 500-600 nm (blue trace), and another weak GSB is resolved (Green trace).

Remarkably the ESA and GSB recovery (shown by the arrow) is an order of magnitude faster in the melanin sample than in melanin-TiO_2. In the melanin sample, the recovery of the ESA occurs in under 10 ps; in melanin-TiO_2, they take several hundred picoseconds. SVD analysis deconvolutes the photoexcited dynamic in spectral and time-domain and further supports the observed electronic interactions between melanin and TiO_2 film and the enhanced charge carrier lifetime due to interfacial charge separation. The discussion on the electronic and chemical structure of melanin and the underlying photophysical processes are provided in the next section 3.6. The observed ultrafast relaxations in melanin nanoparticles in the current study agree with previous laser spectroscopy on melanin polymers measured by time-resolved photoluminescence, and melanin nanoparticles measured by two-color pump-probe spectroscopy. The relaxation of signal in both melanin polymers and nanoparticles was in a few picoseconds.[41,44]

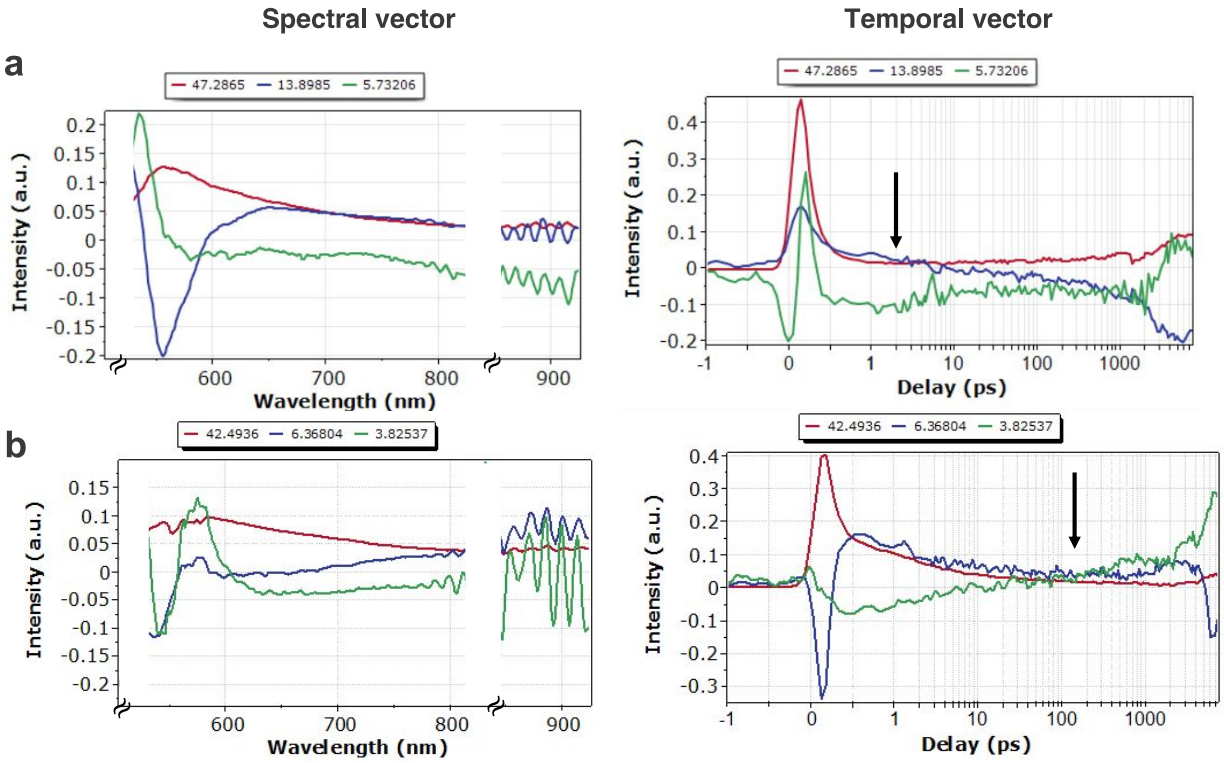

Figure 7. Singular value decomposition on pump-probe transient absorption of melanin nanoparticle-based films, and melanin-TiO_2 films. Data on a) melanin nanoparticles and b) melanin-TiO_2 films. For both samples, the spectral contribution of excited-state absorption, ground-state bleaching, and instantaneous signal at the pump-probe overlap time is identified. Remarkably, ESA and GSB recovery is an order of magnitude faster in the melanin sample than in the melanin-TiO_2. In melanin, GSB and ESA recovery occur in less than 10 ps, while in melanin-TiO_2, the same processes occur in hundreds of picoseconds (shown by arrow).

3.6 Chemical structure, electronic models, and chemical characteristics of excited state at the melanin and melanin-TiO_2 molecular junction and enhanced photochemical activity

To understand the chemical identity of photoexcited species (ESA and GSB) in melanin we first discuss the structural dependent electronic properties of melanin-based constructs. It is well accepted that the 5,6-dihydroxyindole (DHI) and 5,6-dihydroxyindole-2-carboxylic acid (DHICA) units are the two key building blocks of eumelanin. It has been shown that oxidation of DOPA (the chemical used here to make eumelanin nanoparticles) results in the generation of oligomers with both DHI and DHICA units while oxidation of dopamine (the chemical that is used to make the dopamelanin nanoparticles) primarily leads to the generation of DHI as the monomer unit.[30,45,46]Recent structural models through experimental and computational analysis describe the polymerization of monomeric units based on hierarchical self-assembly.[47] The oligomeric units (protomolecules) are stacked and form aggregated substructures. Further aggregation results in the formation of polymeric nanoparticles. Structural models report that DHI melanin consists of largely planar oligomeric scaffolds. These planar oligomeric structures form graphene-like stacked sheets via π-π interactions.[48] A different structure is proposed for the polymerization of DHICA. The DHICA-based oligomer structures are formed by DHICA rotation of ~ 47° about dihedral interunit bonds which results in the formation of nonplanar structures with low stacking.[30]

The DHI and DHICA monomer and dimer units absorb only the UV. Figure 1c shows the absorbance spectrum of dopamine source before and 3 minutes after starting the oxidation/oligomerization reaction with NaOH. Before oxidation, the absorption peak of dopamine reagent has a maximum at 280 nm, which redshifts to 312 nm, and a peak appears at 430 nm as the oxidation/polymerization reaction begins. Further oxidation-polymerization reaction results in further redshift and increase in amplitude resulting a broadband absorption in UV-NIR region-characteristics of melanin absorption- as shown in Figure 1c. This is in agreement with previous reports on the optical absorption of transient species formed by the oxidation of DHI dimers using pulse radiolytic oxidation experiments.[45] The nature of the broadband absorption is not fully understood but it is generally explained by chemical composition diversity and superposition of inhomogeneously broadened transitions associated with the individual segments in the pigment.[30,45,46] The non-covalent interactions such as stacking of oligomeric units via π-π interactions and packing configuration of oligomeric units have also been suggested to contribute to the extent of electron delocalization and optical absorption at energies below the absorption of monomeric units (i.e., in the Vis-NIR region). Ultrafast laser spectroscopy experiments in this study used 460 nm as the pump. Therefore, the pump beam at 460 nm is not energetically able to excite the monomeric units (monomeric units absorb at shorter wavelengths). The 460 nm- pump instead photoexcites and initiates electronic transitions within oligomeric units and the individual segments with red-shifted optical absorption compared to building blocks resulting in the observed GSB peak at 520nm- 650 nm region in the laser spectroscopy results (Figure 6a) and SVD analysis. According to SVD analysis of melanin nanoparticles, a relatively significant GSB component is inhomogeneously centered at ~550 nm with a relatively less significant GSB-type tail extended above 650 nm. The less significant GSB component in SVD can be related to the bleaching within the structural segments with further, red-shifted absorption. Both the broadband TAS spectrum and the SVD analysis confirm the electronic transition within the individual segments (red-shifted absorption compared to the monomeric units' absorption). The shape of the GSB bleaching correlates with that of the broad optical absorption in the Vis-NIR region that appears in a few minutes after oligomerization/polymerization (Figure 1c- less optical absorption in the NIR region compared to the visible region). In the 520-600 nm, there is a spectral overlap between ESA and GSB. The pure excited state relaxation for melanin nanoparticles (excited at 460 nm) is observed above 600 nm with an ultrafast excited state relaxation within sub-10 picoseconds. For melanin-TiO_2 sample, no GSB peak is observed in the 520-600 nm region in TAS spectrum (Figure 6b). The SVD analysis shows non-significant GSB components. The diminish of GSB can be an indication of interfacial charge transfer between melanin and TiO_2- which resembles the semiconductor-sensitized TiO_2 systems.[27] The longer-lived photoexcitation (excited state absorption due to photocarriers) is also another confirmation of charge transfer. It is well known that photoinjected electrons in TiO_2 can have long lifetimes up to milliseconds time scale.[29,49]

Ultrafast laser spectroscopy results of melanin nanoparticles are in general agreement with the previously reported time-resolved measurements of the melanin family although different laser methods and pigments have been used in this study.[41,44] Warren et. al applied two-color TAS spectroscopy on melanin and reported ultrafast excited state relaxation in 5 picoseconds.[41] Sundstrum et al. reported the optical absorption and excited state characteristics of DHICA monomers and dimers using time-resolved fluorescent studies.[44] They showed the maximum absorption peak occurs between 312 nm and 326 nm depending on the pH. Under UV excitation at 280 nm, they found the fluorescence decay for DHICA monomers to have a long lifetime (~3.5 ns in methanol) that is sensitive to the pH. In contrast, the fluorescence decays of the dimers

become much slower with two lifetimes of ~1 and ~10 picoseconds. The very efficient excited state deactivation process in the dimer does not evolve much further when going to the trimer and polymer (i.e. fast relaxation occurs in trimers and polymers as well). The fast and efficient excited state relaxation in melanin is in agreement with results obtained in the current study in which it was found that the majority of excited state relaxation happens in less than 10 ps. The quantum yield of photoluminescence in melanin is reported to be extremely low so that the transient absorption spectroscopy provides a versatile method to study the non-radiative processes. In the current study, the combination of transient absorption laser spectroscopy, SVD analysis, and photochemical analysis using photocatalytic assays comparing the photo-activity of melanin with melanin-TiO_2 donor-acceptor structures sheds light on the photochemistry of melanin and reported melanin-based donor-acceptor structures. The results reported in this study lead to the conclusion that charge carrier processes and the interfacial charge separation are responsible for the observed enhanced relaxation lifetimes, diminished GSB, and improved photocatalytic performance in melanin-TiO_2 donor-acceptor junctions.

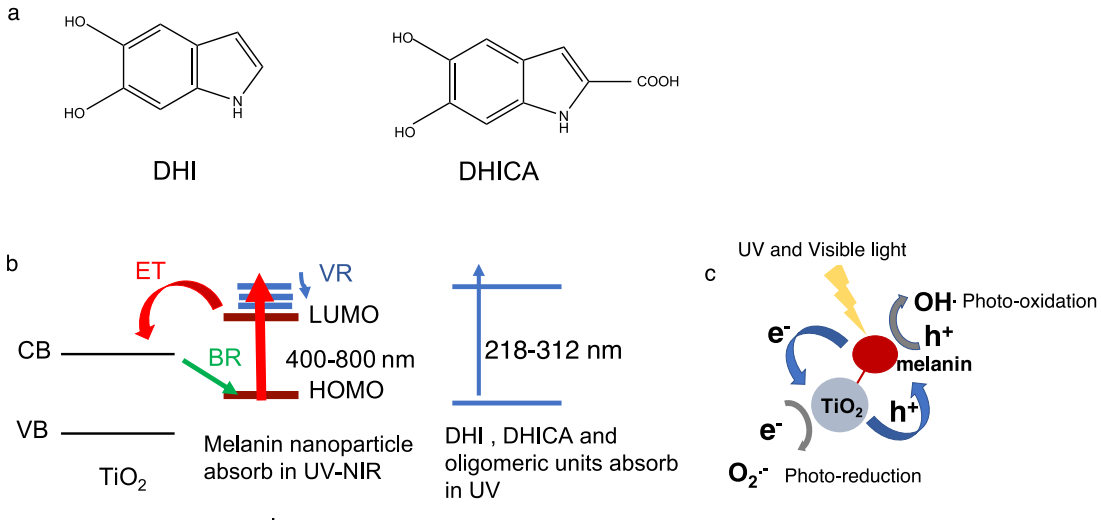

Scheme 1. Chemical structure of melanin monomeric units, melanin nanoparticles-TiO_2 structures, interfacial charge separation, and pathways for photo redox processes. a) Chemical structure of melanin monomeric units DHI and DHICA. b) melanin-sensitized TiO_2 energy levels and interfacial electron transfer processes; schematic of the energy levels of melanin (nanoparticles and oligomeric units) and the electron-acceptor layer (TiO_2). c) Steady-state photocatalytic experiments supported by the direct validation of ultrafast laser spectroscopy show that anchoring melanin on TiO_2 results in charge separation at their molecular junction.

Nanostructured TiO_2 and ZnO are known as excellent large bandgap photocatalyst nanomaterials due to their low cost, ready availability, high chemical and thermal stability, and non-toxic and environmental friendliness.[25,35,50,34,51,52] The semiconductor photocatalytic properties have been reported using photocatalytic degradation studies of organic compounds and dyes. During the photocatalysis process a photon of energy ($\lambda \leq 380$nm) absorbed by metal-semiconductor TiO_2, results in e−/h+ pair generated at (VB-h^+) valence band (VB-h^+) and (CB-e^-) conduction band. The formation of free radicals is responsible for the oxidation of organic compounds and dyes via the following reactions:

1. $TiO_2 + h\nu\ (UV) \rightarrow e^-_{(CB)} + h^+_{(VB)}$ (reactions 1-10):
2. $h^+_{(VB)} + H_2O \rightarrow H^+ + OH^-$
3. $h^+_{(VB)} + OH^- \rightarrow OH^{\cdot}$
4. $e^-_{(CB)} + O_2 \rightarrow O_2^{\cdot -}$
5. $O_2^{\cdot -} + H^+ \rightarrow H_2O^{\cdot}$
6. $H_2O^{\cdot} + H_2O^{\cdot} \rightarrow H_2O_2 + O_2$
7. $H_2O_2 + O_2^{\cdot -} \rightarrow OH^{\cdot} + OH^- + O_2$
8. $H_2O_2 + h\nu \rightarrow 2OH^{\cdot}$
9. Dye molecule + $OH^{\cdot} \rightarrow$ An intermediate compound
10. Intermediate compound $\rightarrow CO_2 + H_2O$

In the presence of melanin and under UV and Vis-NIR irradiation, the following reactions can occur as the initial steps in light absorption and charge separation:

1. $Melanin - TiO_2 + h\nu\ (\text{UV and Vis} - \text{NIR}) \rightarrow e^-_{(melanin)} + h^+_{(melanin)}$ (reactions 1′-4′):
2. $e^-_{(melanin)} + TiO_2 \rightarrow e^-_{(CB - TiO_2)}$
3. $h^+_{(melanin)} + OH^- \rightarrow OH^{\cdot}$
4. $e^-_{(CB - TiO_2)} + O_2 \rightarrow O_2^{\cdot -}$

For melanin-TiO_2 structures, the sample absorbs the photon energy in the UV-NIR region due to the broad absorption of melanin. We have observed enhanced photocatalytic performance in melanin-TiO_2 compared to pure melanin (Figures 4,5). Note that this photocatalytic improvement over pure melanin is observed under both UV-NIR and Vis-NIR irradiation. The improvement cannot be assigned to TiO_2 photoactivity for two reasons: (1) the TiO_2 film is covered by melanin; and (2) TiO_2 is active only in UV, while the photocatalytic improvement is also observed when UV is excluded. Given that both melanin and melanin-TiO_2 samples absorb the same amount of light in Vis-NIR (same amount of melanin in both films), the improved photoactivity of melanin-TiO_2 compared to that of melanin (especially in Vis-NIR) points to interfacial charge separation at melanin-TiO_2 junction that results. An electrochemical method, cyclic voltammetry, was used to investigate melanin's redox characteristics in different electrolytes, and a broad reduction signature observed between 0.4 V and -0.5 V suggests melanin is electron-rich and appropriate for reduction reactions.[53] The extended TAS signal relaxation observed by both ultrafast laser spectroscopy and SVD deconvoluted data analysis confirm longer charge-carrier lifetime in melanin-TiO_2 compared to melanin which support the superior photocatalytic activity of the melanin-TiO_2 film. Scheme 1 shows the interfacial charge separation and the photocatalytic activity of the melanin-TiO_2. Our previous results using laser flash photolysis show that photoinjected electrons in dye-sensitized transparent TiO_2 mesoporous film (the same TiO_2 that is also used in this study) are ling-lived with milliseconds lifetime.[29,54]

While melanin has been mainly looked at as a photoprotectant for many years, recent studies shed more light on the photoactivity of this pigment. It has been reported that after UV exposure; mainly UVA (315-400 nm) and UVB (280-315 nm), melanin can both absorb and release reactive oxygen species (ROS) and induce oxidative stress damage to DNA making melanin a double-faced molecule. Superoxide is the immediate ROS formed after melanin photoexcitation in the presence of oxygen. More phototoxicity has been reported for pheomelanin compared to eumelanin. [55,56] Our photocatalysis experiments are conducted in longer wavelengths (460 nm) and we still see some photoactivity in the degradation of MB pigments for melanin nanoparticles. By anchoring

melanin to TiO_2 (a biocompatible pigment) the photoactivity is even improved. The design of D-A junctions based on melanin can be important to control photochemistry and photocatalytic characteristics.

Despite widespread interest in melanin and melanin derivatives, we know little about the fundamental electron transfer and transport processes in this material family. Our ultrafast TAS studies are sensitive to both radiative and non-radiative transitions on the melanin nanoparticles (polymerized forms of oligomeric units) and point to short-lived charge carriers. Our results have intriguing implications for opto- and bioelectronic applications.

4. Conclusions

In summary, we developed thin films composed of synthetic melanin nanoparticles based on molecular D-A junctions. We conjugated eumelanin and dopamelanin nanoparticles of uniform size and controlled chemical composition to n-type TiO_2 as bilayers. We used inkjet printing to precisely control the melanin deposited for making donor-acceptor junctions. Controlled deposition of melanin is important here for two reasons; to have minimum ink waste as synthesized melanin is an expensive ink and to have reproducible constructs to compare the photocatalytic activities over several tests. We compared the photocatalytic degradation of MB in these melanin-TiO_2 films and pure melanin films (under both UV-NIR and Vis-NIR irradiation) and ascribe its enhancement in the former to a photosensitization effect. Broadband ultrafast spectroscopy results show that about 80% of charge carriers are recombined a few picoseconds after excitation in melanin but live much longer in melanin-anchored TiO_2 films for hundreds of picoseconds. The ultrafast laser spectroscopy studies and quantified data analysis using singular value decomposition provide mechanistic insights into the photochemical characteristics of the melanin and melanin-TiO_2 nanostructured constructs. The enhanced photoexcited lifetime (charge carrier lifetime) due to interfacial charge separation strongly supports the observed photocatalytic activity of melanin-TiO_2.

For many years, melanin has been viewed as a photoprotectant that dissipates most of the irradiation energy. Our laser spectroscopy studies of melanin nanoparticles identify short-lived carriers in melanin, while practical applications would require a strategy to extend the excited state lifetime. The observed photosensitization and interfacial charge separation indicate an extended charge-carrier lifetime in our melanin-based donor-acceptor constructs. The longer-lived-charge carriers in the melanin-TiO_2 nanostructured constructs are of critical importance for future target applications; broadly from biocompatible bioelectronics to photocatalysis and energy conversion devices. However, to optimize them, future studies must optimize the morphology of the melanin-based construct.

Authors' contributions. M. DeMarco performed all photocatalysis experiments using eumelanin nanoparticles and parts of dopamelanin studies, and E. Grage performed photocatalysis experiments using dopamelanin-based samples. M. Ballard synthesized and characterized eumelanin and dopamelanin nanoparticles. F. Nourigheimasi helped with the SVD analysis and parts of the laser experiments. L. Getter helped with thin film preparations and characterizations. A. Shafiee conducted inkjet printing. E. Ghadiri directed the research by conceptualization, funding acquisition, project administration, parts of laser experiments, and wrote the manuscript.

Conflict of interest. There are no conflicts to declare.

Acknowledgments. The support by National Science Foundation (award number 2239539) is greatly acknowledged. The authors would like to thank the WFU Center for Functional Materials and WFU Office of Research and Sponsored Programs for pilot grant support. E. Grage and M. DeMarco acknowledge the undergraduate students' summer fellowship respectively in summer 2019 and summer 2020 supported by WFU-URECA program. We thank M. Guthold and N. Alharbi for their help measuring sample thickness with AFM. We thank S. Day for helping with the XRD measurements. We thank A. Lachgar for proofreading comments.

References

(1) d'Ischia, M.; Wakamatsu, K.; Napolitano, A.; Briganti, S.; Garcia-Borron, J.-C.; Kovacs, D.; Meredith, P.; Pezzella, A.; Picardo, M.; Sarna, T.; Simon, J. D.; Ito, S. Melanins and Melanogenesis: Methods, Standards, Protocols. *Pigment Cell Melanoma Res.* **2013**, *26* (5), 616–633. https://doi.org/10.1111/pcmr.12121.

(2) d'Ischia, M.; Wakamatsu, K.; Cicoira, F.; Di Mauro, E.; Garcia-Borron, J. C.; Commo, S.; Galván, I.; Ghanem, G.; Kenzo, K.; Meredith, P.; Pezzella, A.; Santato, C.; Sarna, T.; Simon, J. D.; Zecca, L.; Zucca, F. A.; Napolitano, A.; Ito, S. Melanins and Melanogenesis: From Pigment Cells to Human Health and Technological Applications. *Pigment Cell Melanoma Res.* **2015**, *28* (5), 520–544. https://doi.org/10.1111/pcmr.12393.

(3) Del Bino, S.; Duval, C.; Bernerd, F. Clinical and Biological Characterization of Skin Pigmentation Diversity and Its Consequences on UV Impact. *Int. J. Mol. Sci.* **2018**, *19* (9), 2668. https://doi.org/10.3390/ijms19092668.

(4) Ito, S.; Wakamatsu, K. Diversity of Human Hair Pigmentation as Studied by Chemical Analysis of Eumelanin and Pheomelanin: Human Hair Pigmentation. *J. Eur. Acad. Dermatol. Venereol.* **2011**, *25* (12), 1369–1380. https://doi.org/10.1111/j.1468-3083.2011.04278.x.

(5) Sitiwin, E.; Madigan, M. C.; Gratton, E.; Cherepanoff, S.; Conway, R. M.; Whan, R.; Macmillan, A. Shedding Light on Melanins within in Situ Human Eye Melanocytes Using 2-Photon Microscopy Profiling Techniques. *Sci. Rep.* **2019**, *9* (1), 18585. https://doi.org/10.1038/s41598-019-54871-y.

(6) Mostert, A. B.; Powell, B. J.; Pratt, F. L.; Hanson, G. R.; Sarna, T.; Gentle, I. R.; Meredith, P. Role of Semiconductivity and Ion Transport in the Electrical Conduction of Melanin. *Proc. Natl. Acad. Sci.* **2012**, *109* (23), 8943–8947. https://doi.org/10.1073/pnas.1119948109.

(7) Meredith, P.; Bettinger, C. J.; Irimia-Vladu, M.; Mostert, A. B.; Schwenn, P. E. Electronic and Optoelectronic Materials and Devices Inspired by Nature. *Rep. Prog. Phys.* **2013**, *76* (3), 034501. https://doi.org/10.1088/0034-4885/76/3/034501.

(8) Ju, K.-Y.; Lee, Y.; Lee, S.; Park, S. B.; Lee, J.-K. Bioinspired Polymerization of Dopamine to Generate Melanin-Like Nanoparticles Having an Excellent Free-Radical-Scavenging Property. *Biomacromolecules* **2011**, *12* (3), 625–632. https://doi.org/10.1021/bm101281b.

(9) Seagle, B.-L. L.; Rezai, K. A.; Gasyna, E. M.; Kobori, Y.; Rezaei, K. A.; Norris, J. R. Time-Resolved Detection of Melanin Free Radicals Quenching Reactive Oxygen Species. *J. Am. Chem. Soc.* **2005**, *127* (32), 11220–11221. https://doi.org/10.1021/ja052773z.

(10) Rageh, M. M.; El-Gebaly, R. H. Melanin Nanoparticles: Antioxidant Activities and Effects on γ-Ray-Induced DNA Damage in the Mouse. *Mutat. Res. Toxicol. Environ. Mutagen.* **2018**, *828*, 15–22. https://doi.org/10.1016/j.mrgentox.2018.01.009.
(11) Chung, S.; Cho, K.; Lee, T. Recent Progress in Inkjet-Printed Thin-Film Transistors. *Adv. Sci.* **2019**, *6* (6), 1801445. https://doi.org/10.1002/advs.201801445.
(12) Molina-Lopez, F.; Gao, T. Z.; Kraft, U.; Zhu, C.; Öhlund, T.; Pfattner, R.; Feig, V. R.; Kim, Y.; Wang, S.; Yun, Y.; Bao, Z. Inkjet-Printed Stretchable and Low Voltage Synaptic Transistor Array. *Nat. Commun.* **2019**, *10* (1), 2676. https://doi.org/10.1038/s41467-019-10569-3.
(13) Xiang, C.; Wu, L.; Lu, Z.; Li, M.; Wen, Y.; Yang, Y.; Liu, W.; Zhang, T.; Cao, W.; Tsang, S.-W.; Shan, B.; Yan, X.; Qian, L. High Efficiency and Stability of Ink-Jet Printed Quantum Dot Light Emitting Diodes. *Nat. Commun.* **2020**, *11* (1), 1646. https://doi.org/10.1038/s41467-020-15481-9.
(14) Huckaba, A. J.; Lee, Y.; Xia, R.; Paek, S.; Bassetto, V. C.; Oveisi, E.; Lesch, A.; Kinge, S.; Dyson, P. J.; Girault, H.; Nazeeruddin, M. K. Inkjet-Printed Mesoporous TiO_2 and Perovskite Layers for High Efficiency Perovskite Solar Cells. *Energy Technol.* **2019**, *7* (2), 317–324. https://doi.org/10.1002/ente.201800905.
(15) Shafiee, A.; Kassis, J.; Atala, A.; Ghadiri, E. Acceleration of Tissue Maturation by Mechanotransduction-Based Bioprinting. *Phys. Rev. Res.* **2021**, *3* (1), 013008. https://doi.org/10.1103/PhysRevResearch.3.013008.
(16) Norotte, C.; Marga, F. S.; Niklason, L. E.; Forgacs, G. Scaffold-Free Vascular Tissue Engineering Using Bioprinting. *Biomaterials* **2009**, *30* (30), 5910–5917. https://doi.org/10.1016/j.biomaterials.2009.06.034.
(17) Shafiee, A.; Norotte, C.; Ghadiri, E. Cellular Bioink Surface Tension: A Tunable Biophysical Parameter for Faster Maturation of Bioprinted Tissue. *Bioprinting* **2017**, *8*, 13–21. https://doi.org/10.1016/j.bprint.2017.10.001.
(18) Shafiee, A.; Ghadiri, E.; Williams, D.; Atala, A. Physics of Cellular Self-Assembly– a Microscopic Model and Mathematical Framework for Faster Maturation of Bioprinted Tissues. *Bioprinting* **2019**, *14*, e00047. https://doi.org/10.1016/j.bprint.2019.e00047.
(19) Shafiee, A.; Ghadiri, E.; Mat Salleh, M.; Yahaya, M.; Atala, A. Controlling the Surface Properties of an Inkjet-Printed Reactive Oxygen Species Scavenger for Flexible Bioelectronics Applications in Neural Resilience. *IEEE J. Electron Devices Soc.* **2019**, *7*, 784–791. https://doi.org/10.1109/JEDS.2019.2910748.
(20) Kwon, Y.-T.; Kim, Y.-S.; Kwon, S.; Mahmood, M.; Lim, H.-R.; Park, S.-W.; Kang, S.-O.; Choi, J. J.; Herbert, R.; Jang, Y. C.; Choa, Y.-H.; Yeo, W.-H. All-Printed Nanomembrane Wireless Bioelectronics Using a Biocompatible Solderable Graphene for Multimodal Human-Machine Interfaces. *Nat. Commun.* **2020**, *11* (1), 3450. https://doi.org/10.1038/s41467-020-17288-0.
(21) McManus, D.; Vranic, S.; Withers, F.; Sanchez-Romaguera, V.; Macucci, M.; Yang, H.; Sorrentino, R.; Parvez, K.; Son, S.-K.; Iannaccone, G.; Kostarelos, K.; Fiori, G.; Casiraghi, C. Water-Based and Biocompatible 2D Crystal Inks for All-Inkjet-Printed Heterostructures. *Nat. Nanotechnol.* **2017**, *12* (4), 343–350. https://doi.org/10.1038/nnano.2016.281.
(22) Ballard, M.; Shafiee, A.; Grage, E.; DeMarco, M.; Atala, A.; Ghadiri, E. Inkjet Printing of Synthesized Melanin Nanoparticles as a Biocompatible Matrix for Pharmacologic Agents. *Nanomaterials* **2020**, *10* (9), 1840. https://doi.org/10.3390/nano10091840.

(23) Shafiee, A.; Ghadiri, E.; Atala, A. Pixel-Based Drug Release System: Achieving Accurate Dosage and Prolonged Activity for Personalized Medicine. *Med. DEVICES Sens.* **2020**, *3* (4), e10104. https://doi.org/10.1002/mds3.10104.

(24) Boehm, R. D.; Miller, P. R.; Daniels, J.; Stafslien, S.; Narayan, R. J. Inkjet Printing for Pharmaceutical Applications. *Mater. Today* **2014**, *17* (5), 247–252. https://doi.org/10.1016/j.mattod.2014.04.027.

(25) Ghadiri, E.; Taghavinia, N.; Aghabozorg, H. TiO_2 Nanotubular Fibers Sensitized with CdS Nanoparticles. *Eur. Phys. J. - Appl. Phys.* **2010**, *50* (2), 20601. https://doi.org/10.1051/epjap/2010025.

(26) Hagfeldt, A.; Boschloo, G.; Sun, L.; Kloo, L.; Pettersson, H. Dye-Sensitized Solar Cells. *Chem. Rev.* **2010**, *110* (11), 6595–6663. https://doi.org/10.1021/cr900356p.

(27) Kamat, P. V. Quantum Dot Solar Cells. Semiconductor Nanocrystals as Light Harvesters. *J. Phys. Chem. C* **2008**, *112* (48), 18737–18753. https://doi.org/10.1021/jp806791s.

(28) Ghadiri, E.; Liu, B.; Moser, J.-E.; Grätzel, M.; Etgar, L. Investigation of Interfacial Charge Separation at PbS QDs/(001) TiO_2 Nanosheets Heterojunction Solar Cell. *Part. Part. Syst. Charact.* **2015**, *32* (4), 483–488. https://doi.org/10.1002/ppsc.201400210.

(29) Ghadiri, E.; Taghavinia, N.; Zakeeruddin, S. M.; Grätzel, M.; Moser, J.-E. Enhanced Electron Collection Efficiency in Dye-Sensitized Solar Cells Based on Nanostructured TiO_2 Hollow Fibers. *Nano Lett.* **2010**, *10* (5), 1632–1638. https://doi.org/10.1021/nl904125q.

(30) Panzella, L.; Gentile, G.; D'Errico, G.; Della Vecchia, N. F.; Errico, M. E.; Napolitano, A.; Carfagna, C.; d'Ischia, M. Atypical Structural and π-Electron Features of a Melanin Polymer That Lead to Superior Free-Radical-Scavenging Properties. *Angew. Chem. Int. Ed.* **2013**, *52* (48), 12684–12687. https://doi.org/10.1002/anie.201305747.

(31) Ito, S.; Murakami, T. N.; Comte, P.; Liska, P.; Grätzel, C.; Nazeeruddin, M. K.; Grätzel, M. Fabrication of Thin Film Dye Sensitized Solar Cells with Solar to Electric Power Conversion Efficiency over 10%. *Thin Solid Films* **2008**, *516* (14), 4613–4619. https://doi.org/10.1016/j.tsf.2007.05.090.

(32) Ghadiri, E.; Zakeeruddin, S. M.; Hagfeldt, A.; Grätzel, M.; Moser, J.-E. Ultrafast Charge Separation Dynamics in Opaque, Operational Dye-Sensitized Solar Cells Revealed by Femtosecond Diffuse Reflectance Spectroscopy. *Sci. Rep.* **2016**, *6* (1), 24465. https://doi.org/10.1038/srep24465.

(33) Derby, B. Inkjet Printing of Functional and Structural Materials: Fluid Property Requirements, Feature Stability, and Resolution. *Annu. Rev. Mater. Res.* **2010**, *40* (1), 395–414. https://doi.org/10.1146/annurev-matsci-070909-104502.

(34) Xu, C.; Rangaiah, G. P.; Zhao, X. S. Photocatalytic Degradation of Methylene Blue by Titanium Dioxide: Experimental and Modeling Study. *Ind. Eng. Chem. Res.* **2014**, *53* (38), 14641–14649. https://doi.org/10.1021/ie502367x.

(35) Bauer, C.; Banerji, N.; Wielopolski, M.; Jonghe, J. D.; Ghadiri, E.; Marchioro, A.; Punzi, A.; Brauer, J. C.; Teuscher, J.; Moser, J.-E. Dynamics and Mechanisms of Interfacial Photoinduced Electron Transfer Processes of Third Generation Photovoltaics and Photocatalysis. *CHIMIA* **2011**, *65* (9), 704–704. https://doi.org/10.2533/chimia.2011.704.

(36) Clancy, C. M. R.; Simon, J. D. Ultrastructural Organization of Eumelanin from *Sepia Officinalis* Measured by Atomic Force Microscopy. *Biochemistry* **2001**, *40* (44), 13353–13360. https://doi.org/10.1021/bi010786t.

(37) Watt, A. A. R.; Bothma, J. P.; Meredith, P. The Supramolecular Structure of Melanin. *Soft Matter* **2009**, *5* (19), 3754. https://doi.org/10.1039/b902507c.
(38) Glass, K.; Ito, S.; Wilby, P. R.; Sota, T.; Nakamura, A.; Bowers, C. R.; Vinther, J.; Dutta, S.; Summons, R.; Briggs, D. E. G.; Wakamatsu, K.; Simon, J. D. Direct Chemical Evidence for Eumelanin Pigment from the Jurassic Period. *Proc. Natl. Acad. Sci. U. S. A.* **2012**, *109* (26), 10218–10223. https://doi.org/10.1073/pnas.1118448109.
(39) Mbonyiryivuze, A.; Mwakikunga, B.; Dhlamini, S. M.; Maaza, M. Fourier Transform Infrared Spectroscopy for Sepia Melanin. *Phys. Mater. Chem.* **2015**, *3* (2), 25–29.
(40) Liu, D.; Wei, L.; Guo, T.; Tan, W. Detection of DOPA-Melanin in the Dimorphic Fungal Pathogen Penicillium Marneffei and Its Effect on Macrophage Phagocytosis In Vitro. *PLoS ONE* **2014**, *9* (3), e92610. https://doi.org/10.1371/journal.pone.0092610.
(41) Ju, K.-Y.; Fischer, M. C.; Warren, W. S. Understanding the Role of Aggregation in the Broad Absorption Bands of Eumelanin. *ACS Nano* **2018**, *12* (12), 12050–12061. https://doi.org/10.1021/acsnano.8b04905.
(42) Ruckebusch, C.; Sliwa, M.; Pernot, P.; de Juan, A.; Tauler, R. Comprehensive Data Analysis of Femtosecond Transient Absorption Spectra: A Review. *J. Photochem. Photobiol. C Photochem. Rev.* **2012**, *13* (1), 1–27. https://doi.org/10.1016/j.jphotochemrev.2011.10.002.
(43) Schmidt, M.; Rajagopal, S.; Ren, Z.; Moffat, K. Application of Singular Value Decomposition to the Analysis of Time-Resolved Macromolecular X-Ray Data. *Biophys. J.* **2003**, *84* (3), 2112–2129. https://doi.org/10.1016/S0006-3495(03)75018-8.
(44) Corani, A.; Huijser, A.; Gustavsson, T.; Markovitsi, D.; Malmqvist, P.-Å.; Pezzella, A.; d'Ischia, M.; Sundström, V. Superior Photoprotective Motifs and Mechanisms in Eumelanins Uncovered. *J. Am. Chem. Soc.* **2014**, *136* (33), 11626–11635. https://doi.org/10.1021/ja501499q.
(45) Pezzella, A.; Panzella, L.; Crescenzi, O.; Napolitano, A.; Navaratman, S.; Edge, R.; Land, E. J.; Barone, V.; d'Ischia, M. Short-Lived Quinonoid Species from 5,6-Dihydroxyindole Dimers En Route to Eumelanin Polymers: Integrated Chemical, Pulse Radiolytic, and Quantum Mechanical Investigation. *J. Am. Chem. Soc.* **2006**, *128* (48), 15490–15498. https://doi.org/10.1021/ja0650246.
(46) Pezzella, A.; Panzella, L.; Crescenzi, O.; Napolitano, A.; Navaratnam, S.; Edge, R.; Land, E. J.; Barone, V.; d'Ischia, M. Lack of Visible Chromophore Development in the Pulse Radiolysis Oxidation of 5,6-Dihydroxyindole-2-Carboxylic Acid Oligomers: DFT Investigation and Implications for Eumelanin Absorption Properties. *J. Org. Chem.* **2009**, *74* (10), 3727–3734. https://doi.org/10.1021/jo900250v.
(47) Clancy, C. M. R.; Nofsinger, J. B.; Hanks, R. K.; Simon, J. D. A Hierarchical Self-Assembly of Eumelanin. *J. Phys. Chem. B* **2000**, *104* (33), 7871–7873. https://doi.org/10.1021/jp001630q.
(48) Meredith, P.; Sarna, T. The Physical and Chemical Properties of Eumelanin. *Pigment Cell Res.* **2006**, *19* (6), 572–594. https://doi.org/10.1111/j.1600-0749.2006.00345.x.
(49) Brauer, J. C.; Marchioro, A.; Paraecattil, A. A.; Oskouei, A. A.; Moser, J.-E. Dynamics of Interfacial Charge Transfer States and Carriers Separation in Dye-Sensitized Solar Cells: A Time-Resolved Terahertz Spectroscopy Study. *J. Phys. Chem. C* **2015**, *119* (47), 26266–26274. https://doi.org/10.1021/acs.jpcc.5b06911.

(50) Dodoo-Arhin, D.; Asiedu, T.; Agyei-Tuffour, B.; Nyankson, E.; Obada, D.; Mwabora, J. M. Photocatalytic Degradation of Rhodamine Dyes Using Zinc Oxide Nanoparticles. *Mater. Today Proc.* **2021**, *38*, 809–815. https://doi.org/10.1016/j.matpr.2020.04.597.

(51) Kim, M. G.; Lee, J. E.; Kim, K. S.; Kang, J. M.; Lee, J. H.; Kim, K. H.; Cho, M.; Lee, S. G. Photocatalytic Degradation of Methylene Blue under UV and Visible Light by Brookite–Rutile Bi-Crystalline Phase of TiO_2. *New J. Chem.* **2021**, *45* (7), 3485–3497. https://doi.org/10.1039/D0NJ05162D.

(52) Ma, Y.; Wang, X.; Jia, Y.; Chen, X.; Han, H.; Li, C. Titanium Dioxide-Based Nanomaterials for Photocatalytic Fuel Generations. *Chem. Rev.* **2014**, *114* (19), 9987–10043. https://doi.org/10.1021/cr500008u.

(53) Xu, R.; Prontera, C. T.; Di Mauro, E.; Pezzella, A.; Soavi, F.; Santato, C. An Electrochemical Study of Natural and Chemically Controlled Eumelanin. *APL Mater.* **2017**, *5* (12), 126108. https://doi.org/10.1063/1.5000161.

(54) Laskova, B.; Zukalova, M.; Kavan, L.; Chou, A.; Liska, P.; Wei, Z.; Bin, L.; Kubat, P.; Ghadiri, E.; Moser, J. E.; Grätzel, M. Voltage Enhancement in Dye-Sensitized Solar Cell Using (001)-Oriented Anatase TiO_2 Nanosheets. *J. Solid State Electrochem.* **2012**, *16* (9), 2993–3001. https://doi.org/10.1007/s10008-012-1729-0.

(55) Solano, F. Photoprotection versus Photodamage: Updating an Old but Still Unsolved Controversy about Melanin. *Polym. Int.* **2016**, *65* (11), 1276–1287. https://doi.org/10.1002/pi.5117.

(56) Mavridi-Printezi, A.; Menichetti, A.; Guernelli, M.; Montalti, M. The Photophysics and Photochemistry of Melanin- Like Nanomaterials Depend on Morphology and Structure. *Chem. – Eur. J.* **2021**, *27* (66), 16309–16319. https://doi.org/10.1002/chem.202102479.